AT2019dge: a Fast-risng Type Ib Ultra-Stripped Envelope SN

Abstract

We present observations of the hydrogen-deficient optical transient AT2019dge/ZTF18abfcmjw. With a rise to maximum light of $\lesssim 3$ days over two magntiude in g and r-bands, AT2019dge is the most rapidly-rising subluminous Type I supernova (SN) discovered so far. Spectra obtained shortly after discover reveal He II flash emission, with broad He I features developed ~ 12 d after peak luminosity. to-do: more to come. AT2019dge poses chanllenge for existing models of fast-rising SNe.

Keywords: supernovae: general – supernovae: individual (AT2019dge) – surveys

1. Introduction

Type Ibc supernovae (SNe Ibc) are explosions of massive stars that have lost their hydrogen envelopes. Their typical rise time ($t_{\rm rise}$ in the range of 10–25 days) and peak luminosity ($M_{R,\rm peak}$ between -17 and $-19\,$mag) suggest ejecta mass ($M_{\rm ej}$) of 1–5 $M_\odot$ and ^{56}Ni mass ($M_{\rm Ni}$) of 0.1–0.4 $M_\odot$ (Drout et al. 2011; Taddia et al. 2018; Prentice et al. 2019). The relatively low $M_{\rm ej}$ and high rates of SNe Ibc are not compatible with prediction from the evolution of single massive stars, whose mass-loss rates are not high enough to strip most of the outer layers. In contrast, Wolf-Rayet (WR) or helium star descendants of massive stars in close binary systems are thought to be the dominate progenitor for the Ibc population (Smith et al. 2011; Dessart et al. 2012; Lyman et al. 2016). The pre-SN star sheds its envelope by mass transfer to the companion, leaving a final envelope mass of $1 M_\odot$ or more prior to explosion (Yoon et al. 2010).

SNe Ibc with the lowest $M_{\rm ej}$ arise from iron-core collapse of a stellar core that stripped its envelope to a greater extent. This can occur in tight binaries where a helium star transfers mass to a neutron star (NS). Such a scenario was invoked to explain the fast evolution of Type Ic SN 1994I with a carbon-oxygen progenitor star of $\sim 2 M_\odot$ and $M_{\rm ej} \sim 0.9 M_\odot$ (Nomoto et al. 1994). Should the degree of stripping be more extreme, we may expect the so-called *ultra-stripped* envelope SNe with $M_{\rm ej}$ and $M_{\rm Ni}$ on the order of 0.1 $M_\odot$ and 0.01 $M_\odot$, respectively (Tauris et al. 2013, 2015; Suwa et al. 2015). These weak explosions are likely the only channel to the formation of double neutron star (DNS) binaries that are compact enough to merge within a Hubble time due to gravitational wave (GW) radiation (Tauris et al. 2017). Ultra-stripped SNe are therefore progenitors of multi-messenger sources that can be jointly studied by the LIGO/VIRGO/KAGRA network (Abbott et al. 2018) and electromagnetic efforts.

Compared with canonical SNe Ibc, we expext light curves of ultra-stripped SNe to be rapidly-evolving and subluminous due to the small amount of $M_{\rm ej}$ and $M_{\rm Ni}$ produced. Among the group of faint and fast objects, SN2005ek (Drout et al. 2013), SN2010X Kasliwal et al. (2010), as well as some of the calcium-rich gap transients such as iPTF10iuv (Kasliwal et al. 2012) and iPTF16hgs (De et al. 2018a) have been suggested to be good candidates for ultra-stripped SNe (Moriya et al. 2017). However, properties of these objects are also consistent with alternative interpretations, including core-collapse of stars with extended hydrogen-free envelopes (Kleiser & Kasen 2014; Kleiser et al. 2018a,b), and scenarios not related to the explosion of massive stars (Metzger et al. 2009; Shen et al. 2010; Sim et al. 2012; Margalit & Metzger 2016).

The most convincing ultra-stripped event to date is the Type Ic SN iPTF14gqr (De et al. 2018b). Its radioactive-powered emission reveals $M_{\rm ej} \sim 0.2 M_\odot$ and $M_{\rm Ni} \sim 0.05 M_\odot$, whereas the detection of early-time shock cooling signatures pins down its core-collapse origin. Discovered within one day of explosion, iPTF14gqr also demonstrates the importance of early-time observations in securely identify ultra-stripped SNe.

Here we report observations and modelling of the rapidly rising ($t_{\rm rise} \lesssim 3$ d) subluminous ($M_{R,\rm peak} \sim -16.3\,$mag) Type Ib SN AT2019dge (ZTF18abfcmjw) discovered by the Zwicky Transient Facility (ZTF; Bellm et al. 2019a; Graham et al. 2019). AT2019dge provides the second consistent observation of an ultra-stripped SN, and the first helium-rich event in this class. Calculations in this paper assume a ΛCDM cosmology with $H_0 = 70\,{\rm km\,s^{-1}\,Mpc^{-1}}$, $\Omega_m = 0.27$ and $\Omega_\Lambda = 0.73$ (Komatsu et al. 2011). UT times are used throughout the paper. All spectra and photometry also be made avail-

able by the WISeREP repository (Yaron & Gal-Yam 2012).

2. Observations

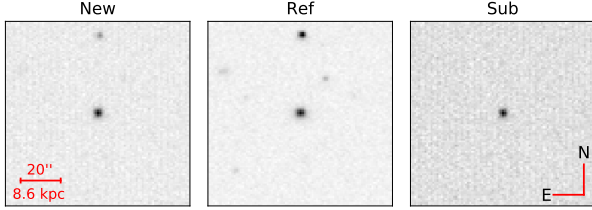### 2.1. The Detection and SN Location

Figure 1. ZTF g band images centered on AT2019dge on Apr 10. From left to right are the new image, the reference image, and the subtraction image.

AT2019dge was first detected by ZTF, which runs on the Palomar Oschin Schmidt 48 inch (P48) telescope. The first real-time alert (Patterson et al. 2019) was generated on 2019 April 7 10:18:46 (JD = 2458580.9297) for a g-band detection at 20.66 ± 0.34 mag and J2000 coordinates $\alpha = 17^{\mathrm{h}}36^{\mathrm{m}}46.75^{\mathrm{s}}$, $\delta = +50^{\mathrm{d}}32^{\mathrm{m}}52.2^{\mathrm{s}}$. On April 8, a new alert was flagged by a science program filter on the GROWTH Marshal (Kasliwal et al. 2019) that is designed to look for fast evolving transients. Figure 1 shows the ZTF detection image on April 10. AT2019dge resildes in a compact galaxy SDSS J173646.73+503252.3 at the redshift of $z = 0.0213$ (See Appendix B.1).

2.2. HST Observation

HST observations are obtained as part of our *Hubble Space Telescope* (*HST*) "Rolling Snapshots" program (GO-15675, Fruchter 2018). This new observational approach requires the PI to update a list of objects of interest each week before the schedule is build, giving
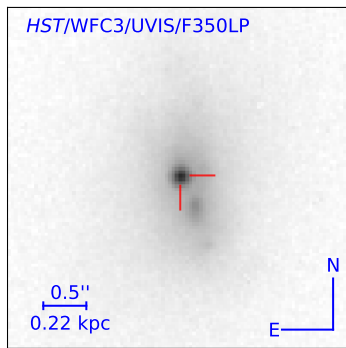

Figure 2. *HST* image of the field on Apr 22 in the F350LP filter. The position of AT2019dge is marked by the red crosshairs.

the scheduler flexibility to choose a possible source of snapshots. Under this program, we obtained a NUV spectrum using the WFC3 G280 grism, a short (60 s) direct image of this field in the F300X filter to set the wavelength scale of the spectrum, as well as a longer exposure (200 s) in the F350LP filter. The image in the F350LP filter is shown in Figure 2. It has very similar throughput to the zeroth order of the G280 grism. We convolved this image to match the slight blurring of the zeroth order G280 grism and then scaled and subtracted it, dramatically reducing host contamination from the zeroth order host image.

Since AT2019dge is offset from the nucleus of the host in Figure 2, the explosion can not be a tidal distrution event.

2.3. Photometry

2.3.1. Optical Photometry

We perform forced PSF photometry on ZTF difference images following the steps illustrated in Yao et al. (2019). The sky region of AT2019dge is covered by two ZTF fields with fieldid 763 and 1799. We exclude all data in field 1799 since the reference image was constructed using images obtained between May 25 2018 and July 12 2019 (see Masci et al. 2019 fordetails of reference image generation), which is after the explosion of the transient. Although the ZTF name of this object (ZTF18abfcmjw) may indicate that the transient was discovered in 2018, this is due to an alert generated on July 7 2018 from a candidate detection in negative subtraction (reference minus science) in field 763. We note that the seeing at that night was 4.2 arcsec, larger than 99% of Palomar nights. The irregular-shaped PSF might caused over-subtraction around the galaxy nucleus in the difference imaging process.

Since field 763 was included in both the northern sky survey with two epochs (one g + one r) per three nights and the extragalactic high-cadence survey with six epochs (three g + three r) per night (see Bellm et al. 2019b for the ZTF experiments design), this transient are visited muliple times every night. Therefore, single-night flux measurements in the same filter are binned (by taking the inverse variance-weighted average). This gives a pre-explosion r-band limit of 18.95 mag (5σ limit computed at the expected position of the transient) on April 4 10:36:34. Five-σ detections are converted to magnitude for further analysis.

Following the discovery of AT2019dge, we obtained follow-up photometry in $griz$ with the optical imager (IO:O) on the Liverpool Telescope (LT; Steele et al. 2004). Digital image subtraction and photometry for LT imaging was performed using the Fremling Automated
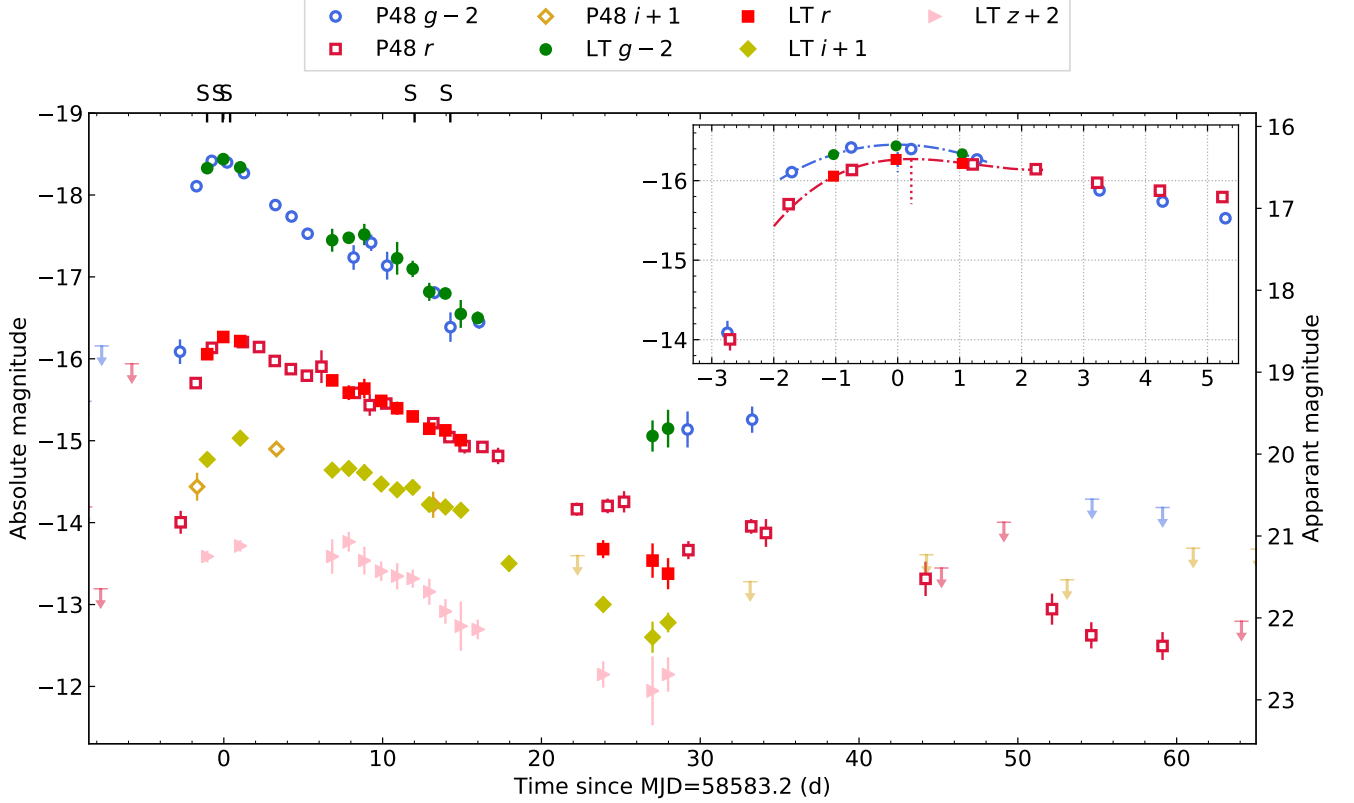
Figure 3. Galactic extinction corrected light curve of AT2019dge. The inset shows the light curve zoomed around the region of maximum light. Epochs of spectroscopy are marked with the letter 'S' along the upper axis.

Pipeline (`FPipe`; Fremling et al. 2016). `Fpipe` performs calibration and host subtraction against Sloan Digital Sky Survey reference images and catalogs (SDSS, Alam et al. 2015).

LT and P48 photometry are shown in Figure 3. Absolute magnitude is determined by correcting for the distance modulus and Galactic extinction $E(B - V) = 0.022$ estimated by Schlafly & Finkbeiner (2011), which builds upon Schlegel et al. (1998). We assume $R_V = 3.1$, and adopt reddening law from Cardelli et al. (1989). We do not correct for host-galaxy contamination given the absence of Na I D absorption in all spectra at the host redshift.

We also performed forced photometry on archival PTF/iPTF difference images spanning May 07 2009 to June 13 2016[1]. No historical detection was found.

2.3.2. Swift Photometry

Space-based observations with the *Neil Gehrels Swift Observatory* (*Swift*; Gehrels et al. 2004) was triggered on April 9 and April 10. Ultraviolet/Optical Telescope

(UVOT; Roming et al. 2005) data were obtained in the $UVW1$, $UVM2$, $UVW2$, U, B, and V filters.

UVOT data are reduced using HEAsoft (v6.17) with a $3''$ circular aperture. To remove host-galaxy contribution at the location of the SN, we obtained a final epoch in all broad-band filters on June 23 2019 and measured the photometry with the same aperture used for the transient. We present a table of our optical and UV photometry in Section A.1.

We note that no point sources were detected in the XRT event files with SNR > 3. The 3σ limits in count s^{-1} in the April 9, April 10, and June 23 observations are 7.8×10^{-3}, 5.8×10^{-3}, and 6.1×10^{-3}, respectively.

2.3.3. Radio Follow-up

Shortly after the discovery of AT2019dge, we initiated radio follow-up in order to constrain the presence of a radio counterpart, as potentially expected in some rapidly-rising transients with circumstellar interaction (Ho et al. 2019a). We observed at high frequency radio bands using the Submillimeter Array (SMA, Ho et al. 2004) on UT 2019 Apr 09 between 15:49:17 and 19:51:26 UTC under its target-of-opportunity program. The project

---

[1] We followed the procedure described in http://web.ipac.caltech.edu/staff/fmasci/home/miscscience/forcedphot.pdf

ID is 2018B-S047 (PI: Anna Ho). We did not detect AT2019dge in the resulting image, while we can place 3σ upper limits to the flux density of $2.25\,\mathrm{mJy}$ at $230\,\mathrm{GHz}$ and $8.4\,\mathrm{mJy}$ at $345\,\mathrm{GHz}$.

2.4. Spectroscopy

We obtained eight optical spectroscopic follow-up of AT2019dge from $-1.1\,\mathrm{d}$ to $+314.4\,\mathrm{d}$ relative to g-band peak using the Rapid Acquisition of Transients (SPRAT; Piascik et al. 2014) on the Liverpool Telescope (LT), the Double Spectrograph (DBSP) on the 200-inch Hale telescope (Oke & Gunn 1982), and the Low Resolution Imaging Spectrograph (LRIS) on the Keck-I telescope (Oke et al. 1995). To extract the LT spectra, we use the automated SPRAT reduction pipeline, which is a modification of the pipeline for FrodoSpec (Barnsley et al. 2012). The DBSP spectrum was reduced using a `PyRAF`-based reduction pipeline (Bellm & Sesar 2016). LRIS spectra were reduced and extracted using `Lpipe` (Perley 2019).

A log of our spectroscopic observations is presented in Appendix B.1. We present our sequence of spectra in Figure 7, Figure 8 and Figure 11.

3. Properties of the Explosion and Its Host Galaxy

3.1. Light Curve Properties

3.1.1. Peak Luminosity, Rise and Decline Timescale

To estimate the epoch of maximum light, we interpolated the g- and r-band photometry with three-order polynomial functions, as is shown in the inset of Figure 3. The time range used in the fit is from MJD = 58581.2 to 58585.2. AT2019dge was found to peak at $M_{g,\mathrm{peak}} = -16.45 \pm 0.04$ mag on MJD = 58583.19, and $M_{r,\mathrm{peak}} = -16.27 \pm 0.02$ mag on MJD = 58583.39. Hereafter we use phase (Δt) to denote time with respect to the g-band maximum light epoch, MJD = 58583.2.

The g- and r-band peak luminosity of AT2019dge (≈ -16.3 mag) is around the lower limit of stripped envelope SNe, and similar to those of the Ca-rich gap transients, which occupy the luminosity 'gap' between novae and SNe (peak absolute magnitude $M_R \approx -15.5$ to -16.5 mag).

To characterize the rise and decline timescales of AT2019dge, we calculate rise time (t_{rise}) defined by how long it takes the r-band light curve to rise from 0.75 mag below peak to peak, and decline time (t_{decay}) determined by how long it takes to decline from peak by 0.75 mag (corresponding to half of maximum flux). In Figure 4 we compare the rise time, decay time, and peak absolute magnitude between AT2019dge and other fast-evolving hydrogen-deficient transients from the literature.
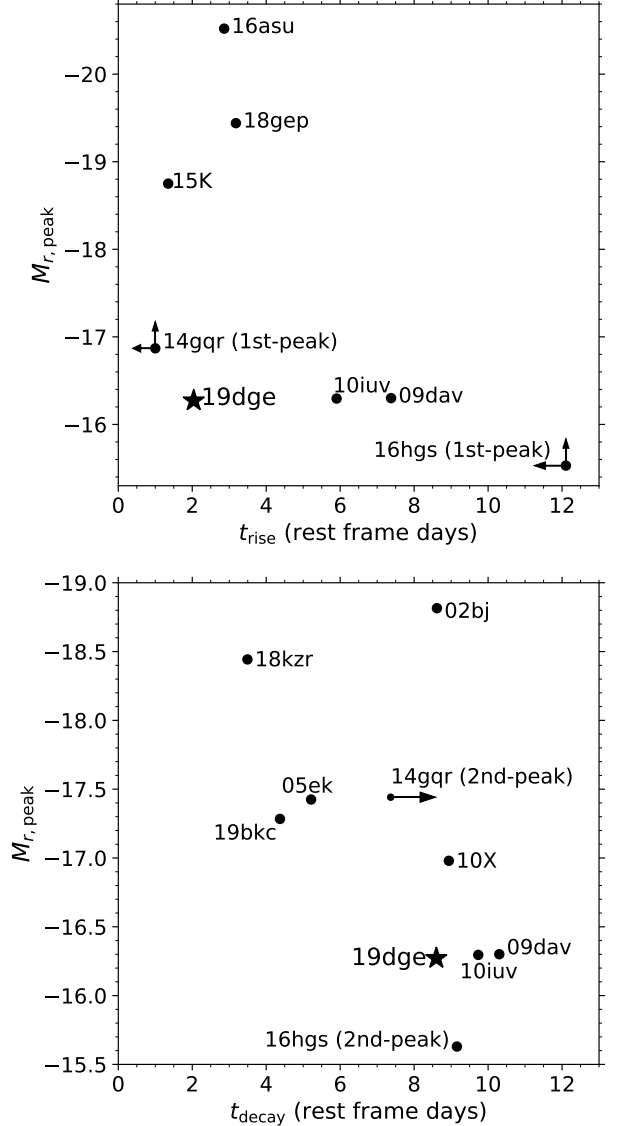

Figure 4. Comparison of the photometric evolution timescales (t_{rise} and t_{decay}) and peak absolute magnitude of AT2019dge to other H-deficient fast-evolving SNe, including SN2002bj (Poznanski et al. 2010), SN2005ek (Drout et al. 2013), PTF09dav (Sullivan et al. 2011), SN2010X (Kasliwal et al. 2010), PTF10iuv (Kasliwal et al. 2012), iPTF14gqr (De et al. 2018b), KSN2015K (Rest et al. 2018), iPTF16asu (Whitesides et al. 2017), iPTF16hgs (De et al. 2018a), SN2018gep (Ho et al. 2019b), SN2018kzr (McBrien et al. 2019), and SN2019bkc (Chen et al. 2020). See the text for details.

In Figure 4, peak magnitudes is given in r-band, except for KSN2015K where we only have observations in the *Kepler* white filter, and iPTF16asu where the rise was only caught in g-band (but in rest-frame r-band since this is a high-redshift event). We only correct for

Galactic extinction to compute $M_{r,\mathrm{peak}}$ (assming no host extinction). Note that iPTF14gqr and iPTF16hgs are two SNe exhibiting double peaked light curves. Since rising of their first peaks were not captured, an upper limit of t_{rise} is calculated by taking the time difference between the first r-band detection and the latest pre-discovery non-detection. Absolute magnitude of the first r-band detection is considered to be a fainter limit of $M_{r,\mathrm{peak}}$ (plotted in the upper panel). In the lower panel, since observation of iPTF14gqr does not extend to 0.75 mag below its second peak, we present a lower limit of its t_{decay}.

It is clear from the upper panel that AT2019dge rose faster than normal Ca-rich events such as PTF09dav and PTF10iuv. The rise time of ≈ 2 d is similar to some fast evolving luminous transients (FELTs) such as KSN2015K, iPTF16asu, and SN2018gep, but AT2019dge is substantially fainter than FELTs. In the subluminous regime, iPTF14gqr and likely iPTF16hgs have t_{rise} comparable to AT2019dge. Their first peaks have been postulated to be caused by the diffusion of shock-deposited energy out of an envelope around the progenitor star (De et al. 2018b,a).

The bottom panel of Figure 4 shows that t_{decay} of AT2019dge is longer than the most rapidly-fading SNe Ibc, such as SN2005ek, SN2018kzr, and SN2019bkc. Its decay timescale is more similar to SN2002bj, SN2010X, the population of Ca-rich transients (PTF09dav, PTF10iuv, iPTF16hgs) and likely iPTF14gqr. It has been suggested that the latter group of events have radioactivity powered main peak with low mass of nickel ($M_{\mathrm{Ni}} \lesssim 0.1 M_{\odot}$).

3.1.2. Bolometric Evolution

We constructed the bolometric light curve evolution by fitting a blackbody function to the spectral energy distribution (SED). At eighteen epochs where at least detections in three flters are available, we utilized the Monte Carlo Markov Chain (MCMC) simulations with `emcee` (Foreman-Mackey et al. 2013) and adopted wide and flat prior for the blackbody radius and temperature ($0 < T_{\mathrm{bb}} < 10^6$ K, $0 < R_{\mathrm{bb}} < 10^6 R_{\odot}$). Uncertainties are estimated using the difference between the 84th and the 16th percentiles of posterior probability distributions. At five epochs that we only have photometric observations in two filters, we fit for T_{bb} and R_{bb} with no estimates on the parameter uncetainies. The SED fits are shown in Appendix A.1.

In Figure 5, we plot the physical evolution of AT2019dge with a comparison to iPTF14gqr and iPTF16hgs. We adopt the explosion epoch of iPTF14gqr, iPTF16hgs, and AT2019dge estimated by
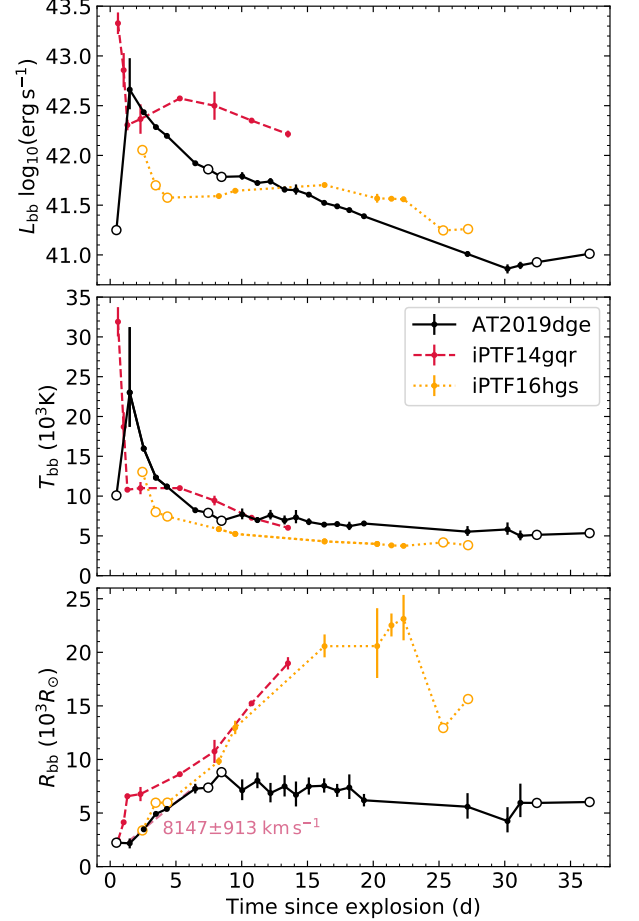

Figure 5. Evolution of blackbody properties (lumionosity, temperature, radius) over time of AT2019dge compared to iPTF14gqr and iPTF16hgs. We adopt blackbody parameters of iPTF14gqr provided by De et al. (2018b), and use the same method as applied in AT2019dge to derive parameters of iPTF16hgs. At epochs where data in more than two filters are available, estimated values are plotted in solid dots, whereas estimates from only two filters are shown in empty circles.

De et al. (2018b), De et al. (2018a), and Section 4.1 of this paper, respectively. The bolometric luminosity of AT2019dge reaches $\sim 5 \times 10^{42}$ erg s^{-1} at ~ 1.5 d after the assumed explosion epoch. The subsequent decline displays an initial fast drop of 0.36 mag d^{-1} at age 2–7 d, and transitions to a slower drop of 0.11 mag d^{-1} at age 8–30 d. Noe that data points of AT2019dge at age 0.5 d are plotted in empty circles, indicating that no uncertainties can be obtained and their values should only be considered as rough estimates.

The bolometric temperature of AT2019dge reaches as high as $\sim 2.3 \times 10^4$ K at age 1.5 d and rapidly falls afterwards. The maximum T_{bb} is much hotter than that observed in normal SNe Ibc (6000–10000 K, Taddia et al.
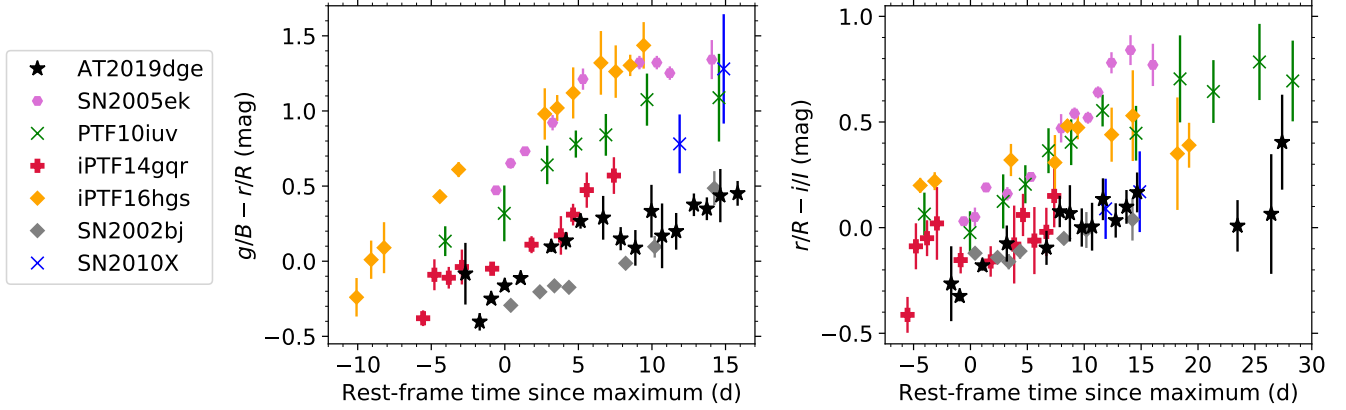
Figure 6. Comparison of the color evolution of AT2019dge with a subset of fast SNe shown in Figure 4. All colors have been corrected for Galactic extincton. Due to absence of photometry in identical filters, we compare colors in corresponding filter pairs of B/g, R/r and I/i.

2018). Its early evolution is less fast than iPTF14gqr, but similar to iPTF16hgs and several other stripped envelope SNe displaying double-peaked light curve (e.g., see Figure 2 of Fremling et al. 2019). Their first peaks have been modelled by cooling emission from an extended envelope around the progenitor after the core-collapse SN shock breaks out (Modjaz et al. 2019). After ~ 8 d past explosion, T_{bb} flattens to 6000 ± 1000 K, similar to the behavior of normal SNe Ibc at a much later phase (~ 30 d after explosion, Taddia et al. 2018).

Assuming that the photospheric radius can be approximated by R_{bb} and linearly expands at early phase, we fit a linear function to the first few R_{bb} vs. time measurements of AT2019dge (lower panel of Figure 5), which gives ≈ 8150 km s^{-1}. The radius remains flat at $\sim 6.6 \times 10^3 R_\odot$ during age 8–30 day, and even appears to slowly recede. The total integrated blackbody energy output during $t = 0.5$–30 d is $\sim 2 \times 10^{43}$ erg s^{-1}.

3.1.3. Color Evolution

We compare the color curves of other fast transients to that of AT2019dge in Figure 6, in corresponding pairs of $B/g - R/r$ and $R/r - I/i$ colors. For double-peaked events iPTF14gqr and iPTF16hgs, "maximum" time corresponds to epoch of maximum light in the second peak.

The early-time blue color of AT2019dge arises from the high-temperature peak. Among other events, SN2002bj, iPTF14gqr and iPTF16hgs exhibit earliest colors as blue as AT2019dge. Subsequently, AT2019dge displays a color starting out blue and turning redder with time, consistent with a cooling process.

One uniqueness of AT2019dge is that at 6–9 days after maximum light, the $g - r$ color becomes bluer by ≈ 0.2 mag, while after that the color continues to redden.

We notice that iPTF14gqr also exhibit this behavior — around 4 day before the second peak, its $g-r$ color stays flat before getting redder afterwards, while around 2 day before the second peak, its $r - i$ color alsp turns bluer by ≈ 0.2 mag.

3.2. Spectroscopic Properties

The phases of the spectra indicated in this section are relative to r-band peak.

3.2.1. Early Spectral Evolution

The very early spectra at -1.1, -0.1, and $+0.4$ d show a blue continuum and strong galaxy emision lines from the underlying H II region (see Figure 7). In addition, these spectra also show prominent He I $\lambda5875$ and high-ionization He II $\lambda4686$ narrow emission lines. Using the line index definition given by Khazov et al. (2016), we calculated the equivalent width of He II to be -7.56 ± 1.07 -2.66 ± 1.30, and -3.77 ± 0.16 in the -1.1 d, -0.1 d, and $+0.4$ d spectra. Full-width at half-maximum intensity (FWHM) velocities of the He II, He I, and Hα emission lines are ~ 550 km s^{-1}, ~ 570 km s^{-1}, and 320 km s^{-1} (unresolved), respectively. Thus, we infer that the hydrogen emission is from the host galaxy, while the helium lines are from photoionized material in a region of immediate environment exterior to the SN.

Early-time low-velocity He II $\lambda4686$ emission has been detected in nearly twenty hydrogen-rich CCSNe and one hydrogen-poor SN iPTF14gqr. This feature often fades away within a few hours to a few days after the explosion (Yaron et al. 2017). The high ionization potential of this line requires high temperature or an ionizing flux, which might come from either shock breakout or CSM interaction (Gal-Yam et al. 2014; Smith et al. 2015). Due to the rapid decrease in T_{bb} at the three epochs of our early-time spectra and the similarity between AT2019dge and
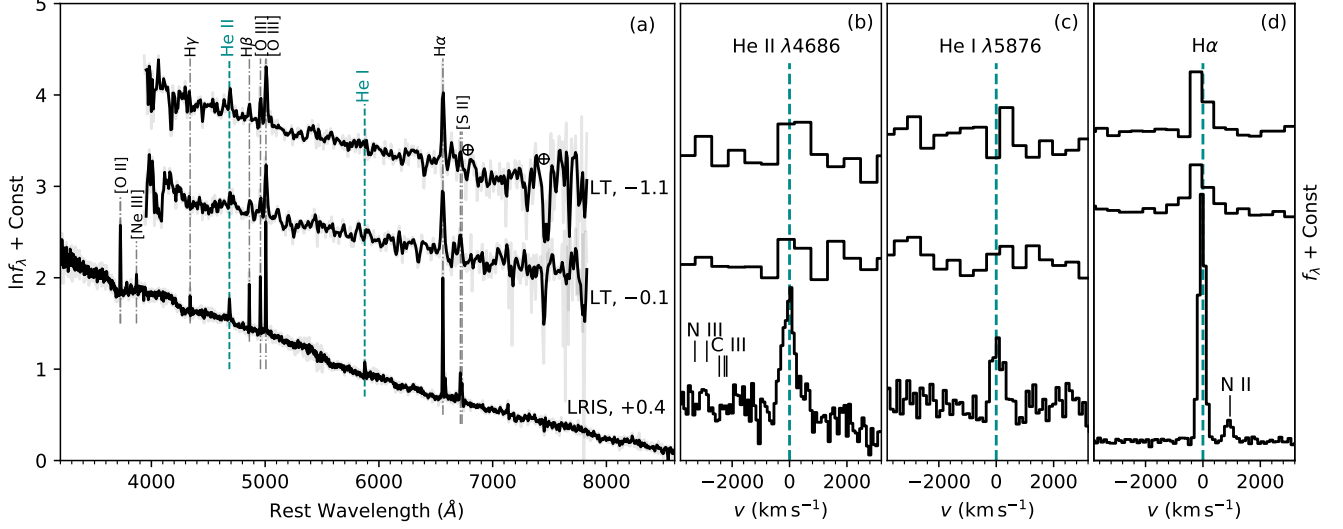
Figure 7. Early-time spectra of AT2019dge. In panel (a), the original spectra are shown in translucent colors, with the overlying black lines showing the same spectra convolved with an FWHM = $800 \, \mathrm{km \, s^{-1}}$ (for LT) or FWHM = $200 \, \mathrm{km \, s^{-1}}$ (for LRIS) Gaussian kernel. Prominent galaxy lines are marked by the dash-dotted lines. In panel (b) (c) and (d), we show the observed spectra (not convolved with any kernels) in velocity space around the He II $\lambda 4686$, He I $\lambda 5876$ and Hα emission lines.
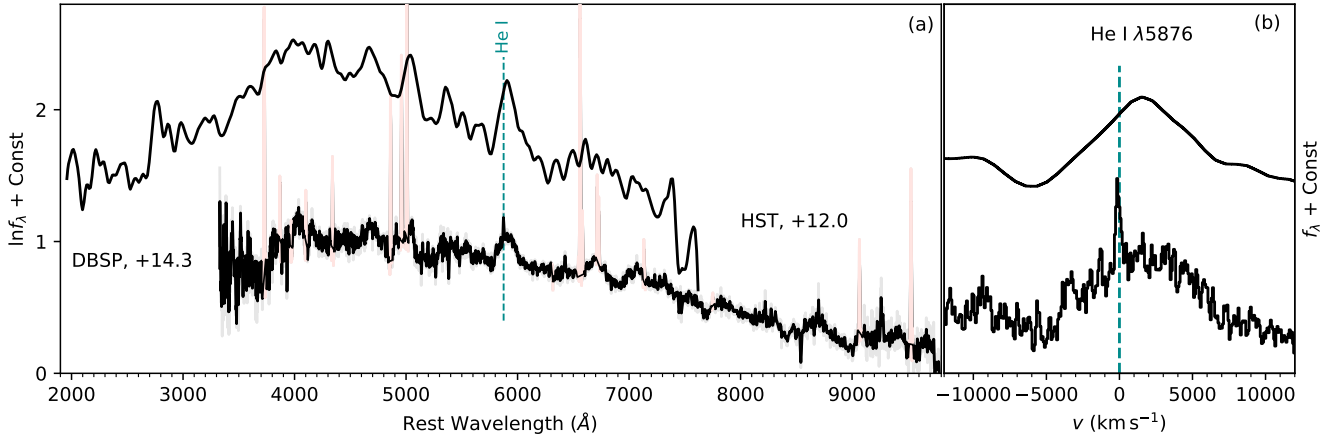

Figure 8. Photosperic phase spectra of AT2019dge. In panel (a), the original DBSP spectrum is shown in translucent colors, with the overlying black lines showing the same spectrum convolved with an FWHM = $200 \, \mathrm{km \, s^{-1}}$ Gaussian kernel. We mask prominent galaxy lines in the DBSP spectrum in light red. In pabel (b), we show the observed spectra (not convolved with any kernels) in velocity space around He I $\lambda 5876$.

iPTF14gqr, we favor shock cooling emission as the origin of recombination helium lines.

3.2.2. Photosperic Phase Spectral Evolution

Broad transient features show up in the +12.0 and +14.3 d spectra (Figure 8). The HST spectrum contains little host-galaxy contamination due to its high angular resolution. Prominent galaxy emission lines in the DBSP spectrum are identified and plotted in light red to emphasize transient features. The existence of P-Cygni He I $\lambda 5876$ profile and non-existence of hydrogen

is reminiscent of Type Ib SN. We measure the velocity of the He I $\lambda 5876$ line by fitting a parabola to the absorption minimum. The resulting fits give velocities of $\approx 6000 \, \mathrm{km \, s^{-1}}$ and $5900 \, \mathrm{km \, s^{-1}}$ for the +12.0 d and +14.3 d spectra, respectively. This is lower than velocities of normal SNe Ib measured from the He I $\lambda 5876$ absorption minimum ($\sim 10^4 \, \mathrm{km \, s^{-1}}$, Liu et al. 2016), but higher than that in Type Ibn SNe ($\sim 3000 \, \mathrm{km \, s^{-1}}$, Hosseinzadeh et al. 2017).

In Figure 9, we compare the photosperic phase optical spectra of AT2019dge with other helium-rich events.
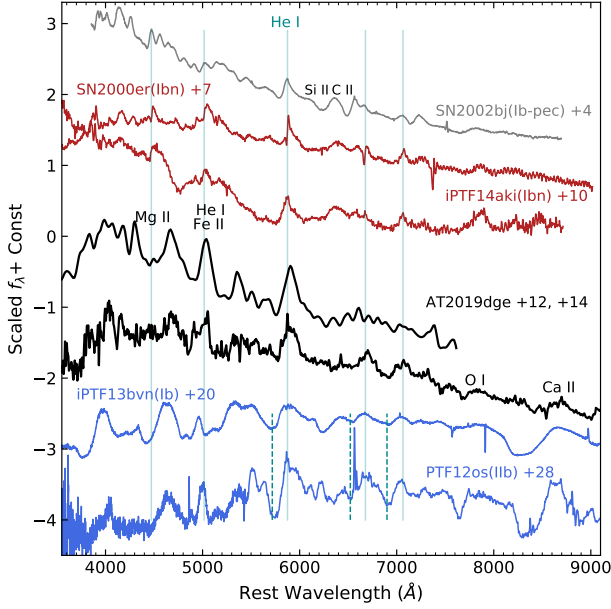
Figure 9. Photosperic phase spectra of AT2019dge compared with other SNe, including SN2000er (Pastorello et al. 2008), SN2002bj (Poznanski et al. 2010), iPTF14aki (Hosseinzadeh et al. 2017), PTF12os and iPTF13bvn (Fremling et al. 2016). He I transitions at rest wavelength are marked by the vertical cyan lines (though note that not all of these lines are visible in all spectra shown here).
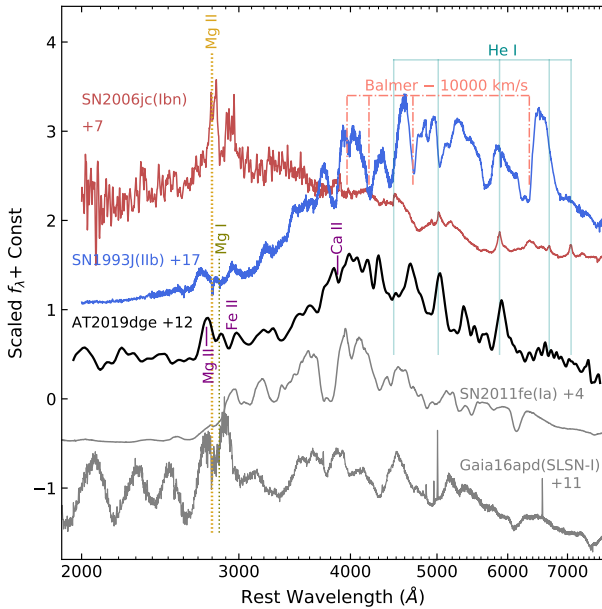

Figure 10. HST spectrum of AT2019dge compared with other SNe, including SN2006jc (Bufano et al. 2009), SN1993J (Jeffery et al. 1994), SN2011fe (Mazzali et al. 2014), and Gaia16apd (Yan et al. 2017).

Note that the DBSP specrum has host emission lines masked. AT2019dge is different from normal helium-rich stripped envelope SNe Ib/IIb or SNe Ibn in the sense that its P-Cygni absoprtion minimum in the He I $\lambda5876$ line is much weaker. The feature at ~ 5000Å is often attributed to He I $\lambda5016$ and Fe II triplet $\lambda\lambda\lambda4924$, 5018, and 5169 (Liu et al. 2016). The shape of this feature in AT2019dge is similar to normal SNe Ib/IIb at much later phase (~ 20 d post maximum), indicating that the spectral evolution of AT2019dge is faster. The complex absorption profile at ~ 4500Å has been identified as a blend of Fe II, Mg II $\lambda4481$ and He I $\lambda4472$ (Hamuy et al. 2002). In the DBSP spectrum, we detected O I $\lambda7774$ and broad Ca II at ~ 8500Å (due to the triplet at 8498, 8542, and 8662Å) with clear P-Cgyni profiles; Both are major features of stripped envelope SNe.

In Figure 10, we compare the HST NUV spectrum with other types of SNe. The UV part of AT2019dge is much weaker than a blackbody extrapolation of the optical spectra would predict. This has also been seen in normal thermonuclear and CCSNe, and interpreted as strong metal-line blanketing caused by iron-peak elements, particularly Fe II and Co II (Gal-Yam et al. 2008). AT2019dge bears a close resembance to SN1993J between 2000 and 4000Å. In Figure 10 we also marked rest wavelength of Mg I $\lambda2852$ and Mg II $\lambda\lambda2796$, 2803. The emission features at ~ 2760Å in AT2019dge and Gaia16apd are similar to the bump at ~ 2730Å in SN1993J, which was found to be a NLTE Mg II emission line (Jeffery et al. 1994). This resonance line is blueshifted from its rest wavelength since the ejecta are very optically thick, and has been interpreted as interaction of the SN ejecta and a circumstellar shell. Such an UV emitting shell may consist of gas originally ejected by the stellar progenitor as a stellar wind or during an episodic mass ejection.

3.2.3. Late-time Spectral Evolution

Panel (a) of Figure 11 shows late time spectra of AT2019dge obtained at $+85.3$, $+143.1$, $+171.1$, and $+314.4$ d. The general shape of the spectra is determined by the host galaxy, while possible SN features are marked by the dashed lines. The right panels (b), (c), and (d) highlight emission lines at wavelengths of He I, [O I], and [Ca II]. FWHM velocities of the narrow emissions are not well resolved ~ 300 km s^{-1}. The intensities decrease by a factor of approximately two from $+85.3$ d to $+314.4$ d. In panel (c), the [O I] $\lambda\lambda6300, 6363$ feature consists of two narrow emission peaks. This doublet transitions share the same upper level ($^3P_{1,2}-^1D_2$). The observed intensity ratio $R \equiv F(6300/6364) \sim 3.1$ agrees with the nebular condition, as one would expect
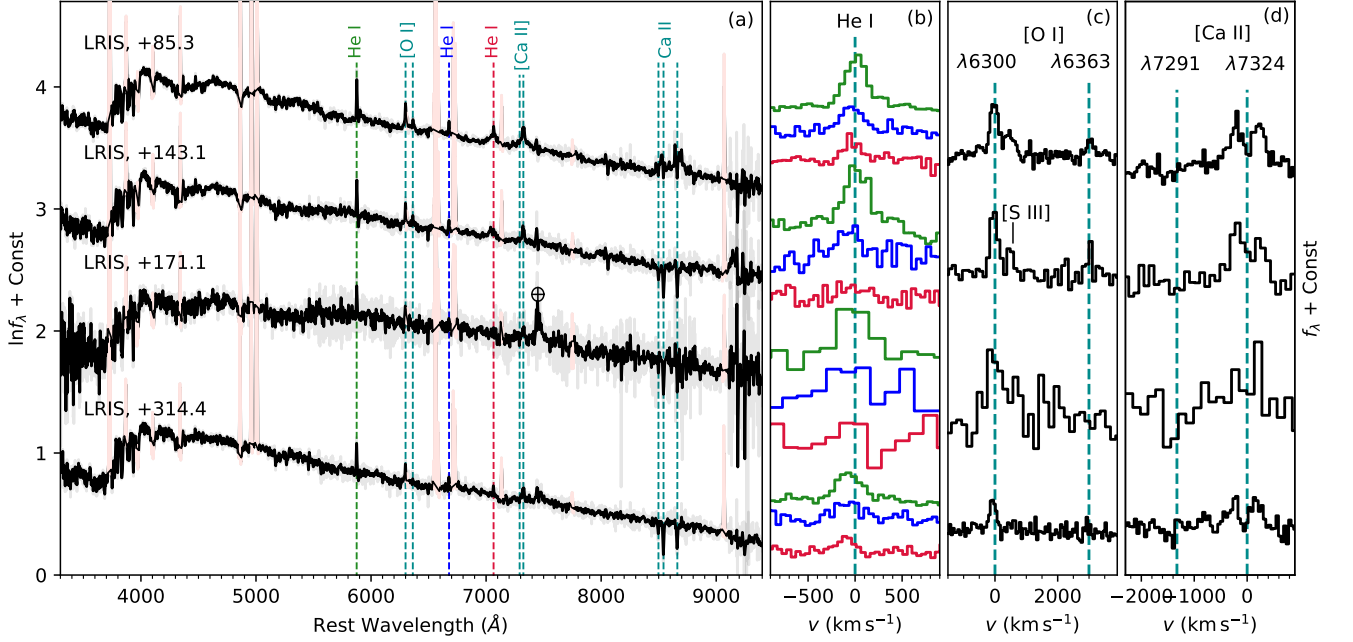
Figure 11. Late-time spectra of AT2019dge. In panel (a), the original spectra are shown in translucent colors, with the overlying black lines showing the same spectra convolved with FWHM = $200\,\mathrm{km\,s^{-1}}$ Gaussian kernels. We mask prominent galaxy lines in light red. Possible SN features are marked by the dashed lines. In panel (b) (c) and (d), the spectra at phase $+85.3\,\mathrm{d}$, $+143.1\,\mathrm{d}$, $+171.1\,\mathrm{d}$, and $+314.4\,\mathrm{d}$, are binned by 1, 2, 3, and 1 pixel(s), respectively. The binning factors are chosen based on the different signal-to-noise ratio (SNR) in these spectra (see exposure times in Table 8). Note that in panel (b), we plot evolution of He I $\lambda5876$, $\lambda6678$, and $\lambda7065$ emissions in green, blue, and crimson, respectively.
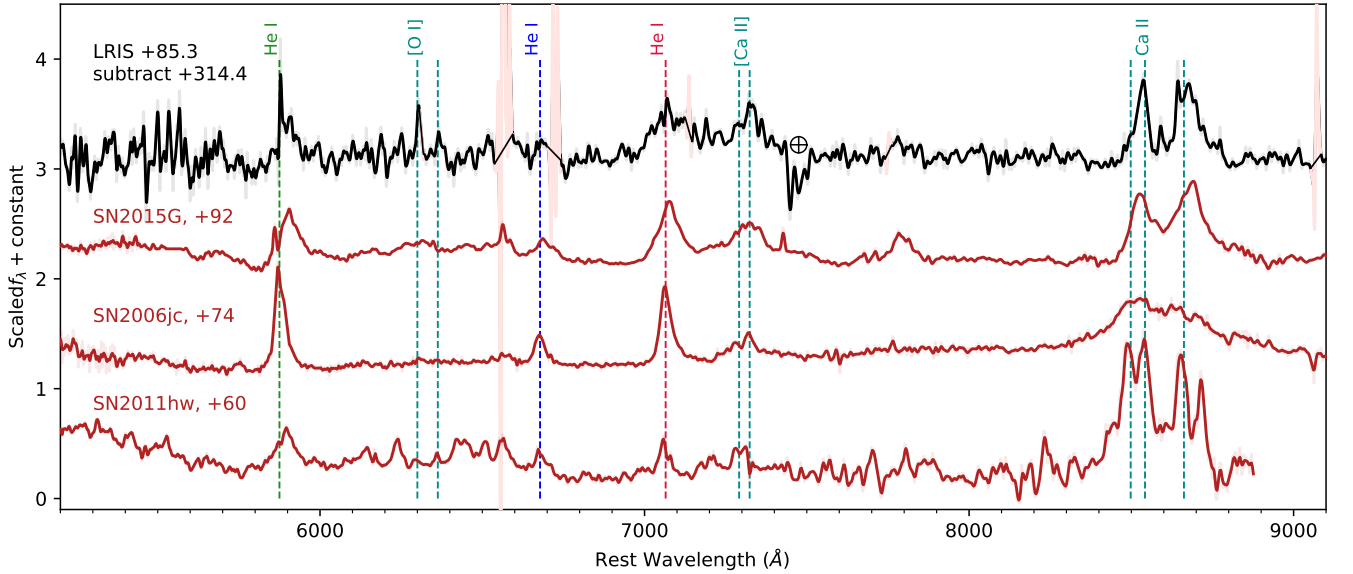

Figure 12. Subtracted nebular spectrum of AT2019dge compared with Type Ibn SNe SN2006jc (Shivvers et al. 2019), SN2011hw (Pastorello et al. 2015), and SN2015G (Shivvers et al. 2017).

in the optically thin regime. In panel (d), we mark position of the [Ca II] $\lambda\lambda7291$, 7324 doublet in dashed lines, but only the $\lambda7324$ line is clearly detected. It presents a double-peaked profile with a peak separation of $\sim 400\,\mathrm{km\,s^{-1}}$.

To further investigate SN features from the galaxy light dominated spectra, we use the $+314.4\,\mathrm{d}$ spectrum as a galaxy template and subtract it from the $+85.3\,\mathrm{d}$ spectrum. The resulting subtraction (Figure 12) reveals intermediate-width (FWHM $\sim 2000\,\mathrm{km\,s^{-1}}$) components of He I, [Ca II], and Ca II IR triplet ($\lambda\lambda\lambda8498$, 8542, 8662), and shares a resemblance to some Type Ibn SNe, such as SN2011hw (Pastorello et al. 2015) and SN2015G (Shivvers et al. 2017). These intermediate-width features are too narrow to be explained by emission from radioactivity-heated optically thin SN ejecta. Instead, they are probably emitted by a dense CSM shell formed by radiative cooling of the post-shock material, as was proposed to be the case in interacting Type IIn/Ibn SNe (Chugai & Danziger 1994; Smith 2017).

The temporal evolution in strength of the narrow ($< 300\,\mathrm{km\,s^{-1}}$) lines shows that the emissions are connected to the explosion and are not merely a background contamination of an underlying H II region. Such narrow lines have been observed at late-time in old nearby CCSNe such as Type Ib Type SN1985F (Filippenko & Sargent 1989), Type IIn SN1986J (Leibundgut et al. 1991) and Type IIb SN1993J (Matheson et al. 2000). They were suggested to arise from dense clumpy regions in the SNe ejecta or circumstellar gas.

pre-shock circumstellar medium (CSM).

Matheson 2001 (Matheson et al. 2001)

The narrow components are not from the ejecta but instead from slow pre-shock CSM

3.3. Host Galaxy Properties

We measure the properties of the host galaxy using the spectrum obtained at phase $+314.4\,\mathrm{d}$, assuming that the nebular line emissions are from the host galaxy.

We infer a star-formation rate of $0.10 \pm 0.02\,M_\odot\,\mathrm{yr^{-1}}$ from the Hα emission line using the Kennicutt (1998) relation converted to use a Chabrier initial mass function (Chabrier 2003; Madau & Dickinson 2014).

We also compute the oxygen abundance using the strong-line metallicity indicator N2 (Pettini & Pagel 2004) with the updated calibration reported in Marino et al. (2013). The oxygen abundance in the N2 scale is 8.23 ± 0.01 (stat) ± 0.05 (sys).

In Figure 13 we shoulw the SED of xx, which was compiled from Swfit/UVOT, SDSS, PS1, 2MASS,, and WISE catalogs. The measured host photometry is given in Table 4.
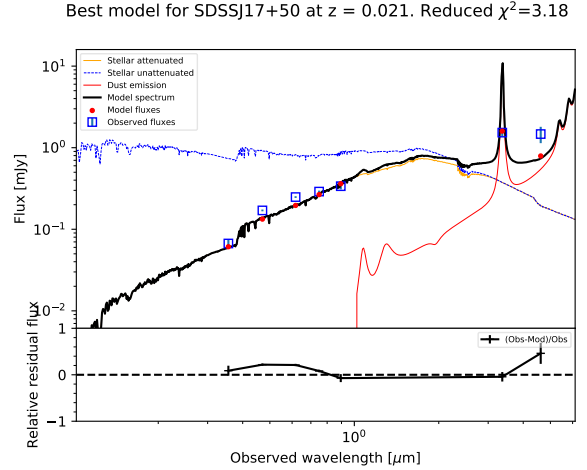

Figure 13. Spectral energy distribution of the host galaxy of AT2019dge. The observed photometric data (with 1σ error bars) are shown in blue open squares, and the model is shown in black curve. The relative residual flux is shown in the bottom panel.

Zhihui: We further determine the stellar mass ($M_\star$) of the host galaxy by SED modeling using CIGALE (Boquien et al. 2019). We adopt the stellar population synthesis models from Bruzual & Charlot (2003) with the Chabrier IMF (Chabrier 2003), and assume a double declining exponential star formation history (SFH). In addition, a dust component is added using the Draine & Li (2007) model to account for dust emission. Finally, the total SED model is attenuated by the Calzetti extinction curve (Calzetti et al. 2000).

The fitted SED is shown in Figure 7. The derived stellar mass is $\log M_\star/M_\odot = 8.0 \pm 0.1$, and the SFR is $0.8 \pm 0.1\,M_\odot\,\mathrm{yr^{-1}}$.

It is worth noting that while several previously reported events (SN 2005ek, SN 2010X, iPTF 14gqr) and SN 2018kzr were found in star forming host galaxies, SN 2019bkc stands out as a hostless transient offset by tens of kpc from any likely host (see Table 1).

Table 1 shows a summary of our literature search.

4. Modelling

4.1. Shock Cooling Powered Fast Rise

to-do: We interpret the AT2019dge's early evolution in the context of shock-cooling emission in Section xx. present evidence 1234

to-do: early blue clor: This serves as another evidence that the early emission of AT2019dge is dominated by shock cooling, as in the case of iPTF14gqr and iPTF16hgs.

to-do: Interestingly, it is also around 6–9 days after maximum that we observed the change in bolometric luminosity decline rate (Figure 5). This further supports

Table 1. Summary of Subluminous Fast Transient.

Name	Redshift	Host	Offset (kpc)	Reference
SN 2002bj	0.012	NGC 1821 (small barred irregular galaxy, $D \sim 1.1$")	1.8 kpc	
SN 2005ek	0.016	UGC 2526 (edge-on spiral galaxy of morphology Sb)	30 kpc	
SN 2010X	0.015	NGC 1573A (small spiral galaxy, $D \sim 1.6$")	2.3 kpc	
iPTF 14gqr	0.063	IV Zw 155 (a tidally interacting spiral galaxy)	29 kpc	De et al. (2018b)
SN 2019bkc	~ 0.02	maybe NGC 3090 (giant elliptical in the MKW1 galaxy group)	~ 94.6	?
AT2019dge	0.021	SDSS J17+50 (small)	0.06 kpc	This work

the idea that the dominate power mechanisms before and after this transition are different.

SNe light cuves are mainly powered by shock energy or radiative diffusion from a heating source. We first examine if the peak of AT2019dge is likely to be powered by the radioactive decay of ^{56}Ni $\to ^{56}$Co $\to ^{56}$Fe. With power a peak luminosity of $L_{\rm peak} \approx 5 \times 10^{42}\,{\rm erg\,s^{-1}}$ and a rise time of $t_{\rm peak} \approx$ 2–4 d, AT2019dge falls into the unshaded region of Kasen (2017, Fig. 1), where an unphysical condition of $M_{\rm Ni} > M_{\rm ej}$ is required. Therefore, we rule out radioactive decay as the power source for the fast rise of the light curve.

Next, we model the early light curve as cooling emission from shock-heated extended material, which locates at the outer layers of the progenitor or outside of the progenitor. We use models presented by Piro (2015, hereafter P15) to constrain the mass and radius of the extanded material ($M_{\rm ext}$ and $R_{\rm ext}$, respectively), where $M_{\rm ext}$ includes only mass concentrated around $R_{\rm ext}$. This model is built on analytical results of Nakar & Piro (2014). Details of the model fitting to multi-band observations are illustrated in Appendix A.2.

In Figure 14, bolometric light curve measured in Section 3.1 are shown in black. We also show late-time r-band νL_ν measurements in grey empty circles as a proxy of bolometric light curve evolution. The dashed green line shows the best-fit model of $M_{\rm ext} = 9.34 \pm 0.36 \times 10^{-2} M_\odot$, $R_{\rm ext} = 2.71^{+0.19}_{-0.17} \times 10^{12}$ cm (i.e., $39.0^{+2.7}_{-2.5} R_\odot$), and first light epoch at phase $t_{\rm fl} = -3.21_{\pm 0.04}$ day (i.e., the explosion occurred 0.45 d before the first detection in g-band). The amount of energy passed into the extended material is well constrained to be $E_{\rm ext} = (1.15 \pm 0.07) \times 10^{50}\,{\rm erg\,s^{-1}}$.

Given the simple assumptions of the model, we expect the constraints on $M_{\rm ext}$ and $R_{\rm ext}$ to be only approximatedly accurate. There are now numerous cases of early cooling envelope emission observed in CCSNe, where the extented matrial is estimated to have lower mass ($\sim$ 0.001–0.01$M_\odot$) and larger radius ($\sim 10^{13}$ cm) compared to AT2019dge (Modjaz et al. 2019). We thus
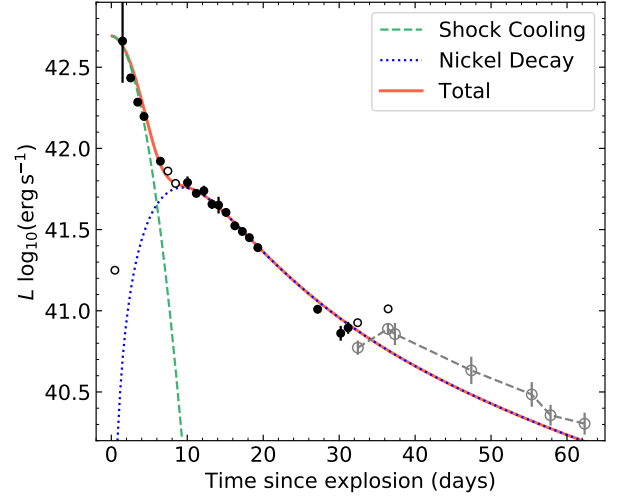

Figure 14. Bolometric light curve for AT2019dge. The quasi-bolometric light curve of AT2019dge estimated by computing νL_ν in r-band is shown as emply grey circles. The dashed green and dotted blue lines show the best fits of shock cooling and nickel decay models. The solid red line shows the combination of the two components.

conclude that the early shock cooling emission was produced by an extended shell (instead of an envelope) with a mass of $\sim 0.1 M_\odot$ locating at a radius of $\sim 3 \times 10^{12}$ cm.

to-do: try to see if puffier helium star produce lower ejecta mass. See eg Fig.16.7: Tauris 2003. However, if it was really 50 Rsun at explosion, it would have been in such a wide binary that it could not have been stripped down to an envelope layer of just 0.3 Msun. This is quite intriguing! How sure are you of a progenitor radius of 50 Rsun? Could this radius instead represent some sort cocoon of helium-rich material ejected shortly before the SN? Even in the case of 14gqr, we saw that the star was too large (500 Rsol) to explain a binary system stripped that much. We had explained this by invoking a short lived common envelope phase just before the explosion where the companion gets engulfed by the expanding He star. This could perhaps be the case here as well.

to-do: rephrase: We conclude that the AT2019dge is not one of FELTs. Its fast $t_{\rm rise}$ is reminiscent of shock cooling emission, and the moderate $t_{\rm decay}$ is consistent with coming from radioactivity.

Table 2. shock P15.

Name	Type	$R_{\rm ext}$ (10^{12} cm)	$M_{\rm ext}$ ($10^{-2} M_\odot$)
iPTF16hgs	Ca-rich	0.9	8
AT2019dge	Ib-pec	$2.69^{+0.34}_{-0.16}$	$9.40^{+0.69}_{-0.33}$
iPTF14gqr	Ic-pec	30^{+3}_{-3}	$0.88^{+0.08}_{-0.07}$
iPTF15dtg	Ic	83	5
SN2016gkg	IIb	$4.00^{+0.05}_{-0.05}$	$2.50^{+0.01}_{-0.01}$
ZTF18aalrxas	IIb	73^{+3}_{-2}	$4.3^{+0.14}_{-0.13}$

NOTE—Reference: iPTF14gqr (De et al. 2018b), SN2016gkg (Arcavi et al. 2017), ZTF18aalrxas(Fremling et al. 2019)

4.2. Mass Loss Estimate from He II

following the procedure given by Ofek et al. (2013) and De et al. (2018b), we use luminosity of the He II $\lambda 4686$ line to make an order-of-magnitude estimate on properties of the emission material. We get radius of the line emitting region $r \gtrsim 4.8 \times 10^{13}\beta$ cm, mass losss parameter $K \gtrsim 1.2 \times 10^{14}$ g cm^{-1}, and helium mass of the emitting region $M_{\rm He} \gtrsim 3.6 \times 10^{-5}\beta^2 M_\odot$, where β is the ratio of the CSM width over radius. Note that these estimates can be affected if the CSM can not be well characterized by a spherically symmetric $\rho(r) \propto r^{-2}$ density profile, or if the emitting region was confined to a thin shell ($\beta \ll 1$).

Assuming that the CSM around the progenitor has a spherical wind-density profile of the form $\rho = Kr^{-2}$, where r is distance from the progenitor, $K \equiv \dot{M}/(4\pi v_{\rm w})$ is the wind density parameter, $v_{\rm w}$ is the wind/outburst velocity, and $\dot{M}$ is the mass loss rate. The integrated mass of the emitting material from r to r_1 is

$$M_{\rm He} = \int_r^{r_1} 4\pi r^2 \rho(r) {\rm d}r = 4\pi K \beta r \qquad (1)$$

where $\beta \equiv (r_1 - r)/r$ is assumed to be of the order unity.

Following De et al. (2018b), we can relate the mass of the He II region to the He II $\lambda 4686$ line luminosity using

$$L_{\lambda 4686} \approx \frac{A n_e M_{\rm He}}{m_{\rm He}}. \qquad (2)$$

Here

$$A = \frac{4\pi j_{\lambda 4686}}{n_e n_{\rm He^{++}}}, \qquad (3)$$

$j_{\lambda 4868}$ (in erg cm^{-3} s^{-1} sr^{-1}) is the emission coefficient for the $\lambda 4686$ transition. $m_{\rm He}$ is mass of a He nucleus, $n_{\rm He^{++}}$ is the number density of doubly ionized helium and n_e is the number density of electrons.

Assuming a temperature of 10^4 K, electron density of 10^{10} cm^{-3}, and Case B recombination, we get $A = 1.32 \times 10^{-24}$ erg cm^3 s^{-1} (Storey & Hummer 1995). Assuming $n_e = 2 n_{\rm He^{++}}$ and using the density profile, Eq. (2) can be written as

$$L_{\lambda 4686} \approx \frac{8\pi A \beta}{m_{\rm He}^2} \frac{K^2}{r}. \qquad (4)$$

The location of the emitting region can be constrained by requiring that the Thompson optical depth (τ) in the region must be small for the lines to escape. We require

$$\tau = n_e \sigma_{\rm T} \int_r^{r_1} {\rm d}r = \frac{2\sigma_{\rm T} K \beta}{m_{\rm He} r} \lesssim 1 \qquad (5)$$

Thus

$$r^2 \gtrsim \left(\frac{2\sigma_{\rm T}\beta}{m_{\rm He}} \right)^2 \frac{L_{\lambda 4686} m_{\rm He}^2 r}{8\pi A \beta}$$

$$r \gtrsim L_{\lambda 4686} \frac{\sigma_{\rm T}^2 \beta}{2\pi A} \qquad (6)$$

The $+0.4$ d emission line flux is meausred to be $F = (8.37 \pm 0.65) \times 10^{-16}$ erg cm^{-2} s^{-1}, correslonding to $L_{\lambda 4686} = 8.6 \times 10^{38}$ erg s^{-1}. Hence, we get $r \gtrsim 4.8 \times 10^{13}\beta$ cm, $K \gtrsim 1.2 \times 10^{14}$ g cm^{-1}, and $M_{\rm He} \gtrsim 3.6 \times 10^{-5}\beta^2 M_\odot$.

4.3. Constraints on Radio Emission

Radio emission in SNe is produced by shock accelerated electrons in the circumstellar material as they gyrate in the post-shock magnetic field when the shock freely expands. Should the circumstellar medium be formed by a pre-SN stellar wind, the radio synchrotron radiation can be used to probe the pre-explosion massloss (Chevalier 1982). High frequency ($\nu > 90$ GHz) bright ($\nu L_\nu \gtrsim 10^{40}$ erg s^{-1}) radio sources are often found to be associated with gamma-ray bursts (GRBs), TDEs, and relativistic transients (see Figure 6 of Ho et al. 2019a). Among normal SNe Ibc, moderate submillimeter luminosity at $\sim 5 \times 10^{37}$ erg s^{-1} has been observed in SN1993J (Weiler et al. 2007) and SN2011dh (Horesh et al. 2013).

Our SMA observations constrain the submillimeter luminosity of AT2019dge to $\nu L_{\nu,230{\rm GHz}} < 5.3 \times 10^{39}$ erg s^{-1} and $\nu L_{\nu,345{\rm GHz}} < 3.0 \times 10^{40}$ erg s^{-1}. Wwe place these upper limits in physical context using the synchrotron self-absorption model given by Chevalier (1998). The expected radio luminosities are computed
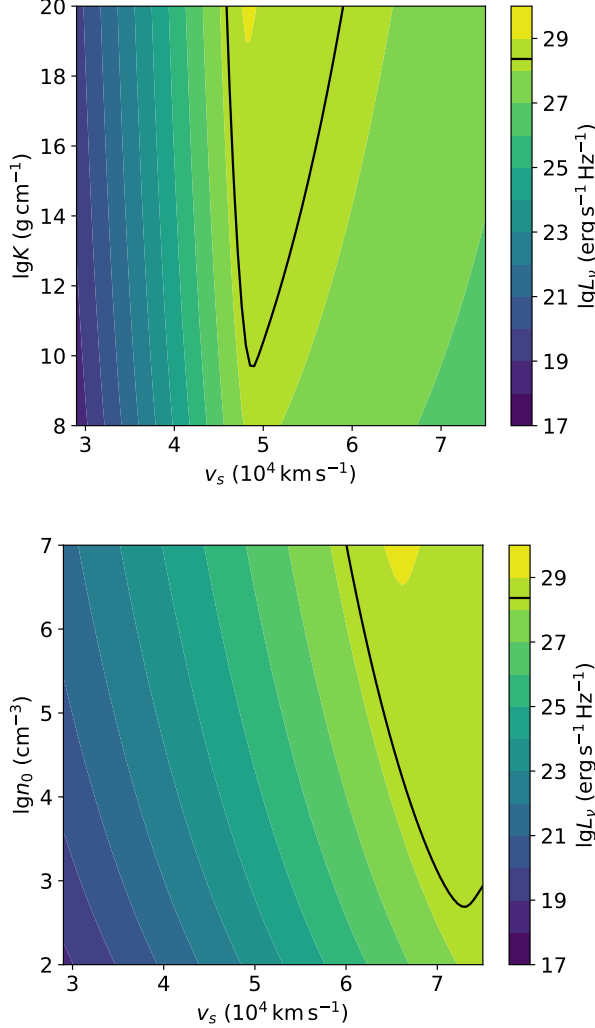
Figure 15. Expected radio luminosity at 230 GHz at different shock velocity v_s and wind mass-loss parameter K in the case of $\rho \propto r^{-2}$ CSM environment (upper panel) or number density n_0 in the constant-density case (bottom panel). The black contour in each panel shows the location of the 3σ upper limit at 230 GHz on AT2019dge. The phase space with a luminosity higher the black line in each panel is ruled out by the observation.

at 230 and 345 GHz for two types of circumstellar environments — one with the wind-density with the same parameterization as that adopted in Section 4.2 and the other with a constant-density environment ($\rho =$ constant).

Adopting the explosion epoch found in Section 4.1, our SMA observations were obtained at 2.75 day after explosion. Given the early time of these observations, we consider constant shock velocities at 0.1–0.25c, as found to be typical in SNe Ibc (Wellons et al. 2012). We assume an electron energy power law index of $p = 3$, a

volume filling factor $f = 0.5$, and that the electrons and magnetic field in the post-shock region share constant fractions of the post-shock energy density, i.e., $\epsilon_e = \epsilon_B = 0.1$.

We show the contour plots (in the phase space of jet energy and circumstellar density) of the expected radio fluxes at the epochs of the VLA and GMRT observations for different viewing angles, along with our limits on the radio emission of this source in Figure 13. We constrain the wind mass-loss parameter K and the external circumstellar density n_0 by obtaining the limiting cases for our 3σ detections, as shown in Figure 15. xx in the wind-CSM case and xx in the constant-ρ case

4.4. Radioactivity Powered Main Peak

After subtracting the shock cooling emission from the bolometric light curve, the remaining light curve has a peak luminosity of $L_{\text{peak}} \approx 6 \times 10^{41} \, \text{erg s}^{-1}$ and a rise time of $t_{\text{peak}} \approx 9 \, \text{d}$. In the shaded region of Kasen (2017, Fig. 1), this falls into the $M_{\text{Ni}} = 0.1 M_{\text{ej}}$ and $M_{\text{Ni}} = 0.01 M_{\text{ej}}$ lines, indicating that the remaining component can be powered by ^{56}Ni decay. Here we use two methods to estimate M_{ej} and M_{Ni}.

First of all, we use analytical models (Arnett 1982; Valenti et al. 2008; Wheeler et al. 2015) to constrain the nickel mass (M_{Ni}), a characteristic photon diffusion timescale (τ_{m}), and a characteristic γ-ray escape timescale (t_0). Details of the model fitting are illustrated in Appendix A.3. The dotted blue line in Figure 14 shows the best-fit model of $M_{\text{Ni}} = 1.69^{+0.05}_{-0.04} \times 10^{-2} M_\odot$, $\tau_{\text{m}} = 7.15 \pm 0.16 \, \text{d}$, and $t_0 = 22.17^{+0.74}_{-0.73} \, \text{d}$. Thus, using Equation (A6), the ejecta mass can be estimated to be

$$M_{\text{ej}} = (0.46 \pm 0.02) M_\odot \frac{v_{\text{ej}}}{8150 \, \text{km s}^{-1}} \frac{0.07 \, \text{cm}^2 \, \text{g}^{-1}}{\kappa_{\text{opt}}}$$

Recently, Khatami & Kasen (2019, hereafter KK19) presents improved analytic relations (compared with the original Arnett 1982 model) between t_{peak} and L_{peak}. When $t < 10 \, \text{d}$, $\varepsilon_{\text{Ni}}(t) \gg \varepsilon_{\text{Co}}(t)$ (see Equations A3, A4), and thus we have an exponential heating function

$$L_{\text{heat}}(t) = L_0 e^{-t/\tau_{\text{Ni}}} \tag{7}$$

where $L_0 = M_{\text{Ni}} \times \epsilon_{\text{Ni}}$. In this case, KK19 (Eq. 21) shows that the relation between peak time and luminosity is:

$$L_{\text{peak}} = \frac{2 L_0 \tau_{\text{Ni}}^2}{\beta^2 t_{\text{peak}}^2} \left[1 - (1 + \beta t_{\text{peak}}/\tau_{\text{Ni}}) e^{-\beta t_{\text{peak}}/\tau_{\text{Ni}}} \right] \tag{8}$$

where $\beta \sim 4/3$ gives a reasonable match to numerical simulations. With $L_{\text{peak}} \approx 6 \times 10^{41} \, \text{erg s}^{-1}$ and $t_{\text{peak}} \approx 9 \, \text{d}$, we get an estimate of $M_{\text{Ni}} \sim 0.018 M_\odot$.

$M_{\rm ej}$ can be estimated using Eq. 23 of KK19:

$$\frac{t_{\rm peak}}{t_{\rm d}} = 0.11 \ln\left(1 + \frac{9\tau_{\rm Ni}}{t_{\rm d}}\right) + 0.36, \qquad (9)$$

where $t_{\rm d}$ is the characteristic timescale without any numerical factors

$$t_{\rm d} = \left(\frac{\kappa_{\rm opt} M_{\rm ej}}{v_{\rm ej} c}\right)^{1/2}. \qquad (10)$$

We derive $t_{\rm d} \approx 16.2$ d, which implies

$$M_{\rm ej} \approx 0.30 M_\odot \frac{v_{\rm ej}}{8150\,{\rm km\,s^{-1}}} \frac{0.07\,{\rm cm^2\,g^{-1}}}{\kappa_{\rm opt}}$$

In conclusion, the estimates derived from simplified modelling fitting and new analytic relations from KK19 are roughly the same. Ejecta mass and nickle mass from the explosion of AT2019dge are very small, $M_{\rm ej} \sim 0.3 M_\odot$, $M_{\rm Ni} \sim 0.02 M_\odot$.

4.5. A Highly Stripped Progenitor in a Binary System

The shock cooling powered early emission followed by the radioactivity powered decay indicates that AT2019dge is associated with the class of iron core-collapse events. The small amout of ejecta mass requires extreme stripping prior to the explosion, and rules out single massive star to be the progenitor. The helium-rich photosperic phase spectra suggests that the bulk of the ejecta should be helium.

The evolution of binary massive stars

Tight helium star–NS binary systems, presumably created in the common-envelope phase from high-mass X-ray binaries, can lead to the extrame stripping of the helium envelope pand result in SNe with ejecta masses of the order of 0.1Msun

Many progenitors are expected to have a helium mass above the critical helium mass (0.1 Msun, Hachingerr 2012) required to observe optical helium features Tauris 2015 and thus may be observed as SN Ib like AT2019dge.

In this picture, the helium-star mass transfer rate is 3–4 orders of magnitude greater than the Eddington accretion rate for NSs and $> 99.9\%$ of the transferred mass is lost from the system (Tauris et al. 2015), forming a shell of $\sim 0.1 M_\odot$ and 3×10^{12} cm at the time of explosion.

to-do: This is actually not ultra-stripped SN: Mej larger than 0.2 Msun. Can form this using HMLB – Case BB RLO – stripp – double NS. OR. Massive star explosion??

5. Discussion

Woosley (2019) shows that mass-losing helium stars with initial masses between 2.5–3.2 $M_\odot$ experience raidus expansion after helium depletion (but lack a strong silicon flash), which gives rise to the early-time shock cooling emission out of the ejected helium envelope. If the explosion makes substantial ^{56}Ni, then the light curve may have two peaks, the second resembling a SN Ib but occurring earlier due to the low $M_{\rm ej}$.

to-do: ask Thomas: discussions on the age of the system (e.g. the time to the 2nd SN in a binary system in relation to a star burst in the host galaxy, and a few words on the subsequent delay time until a merger - in case AT2019dge represents an event where it is the 2nd SN producing a double compact object binary that remains bound).

massive mass-loss episode that takes place just prior to the explosion (Shiode & Quataert 2014)

Progenitor: why so rare??? Could the progenitor be a helium rich WR star, perhaps recently transitioned from an LBV phase

Constraints on event rate?

6. Conclusion

In this paper we have presented observations and modeling of the fast transient AT2019dge. We summarize our primary observational findings below:

(a) Peak absolute magnitude of MB = dd mag and decline parameter of hah mag.

(b) Total Nickel and ejecta masses of $M_{\rm Ni} = 0.02 \pm 0.01$ and $Mej = 0.3 \pm 0.3 M_\odot$, respectively.

(c) spectrum is peculiar

(d) photosperic phase spec emission comes from a photosphere receding (in mass coordinates) back through freely expanding SN ejecta (smith 2016 rewrite)

(e) Ca-rich event nebular spectrum

equatorial CSM deposited by binary interaction (Smith2017)

The combination of depth, cadence and sky coverage offered by ongoing time domain surveys enables detection within one day of the explosion, opening a new window into the relatively unexplored early phase of these events.

Enhanced (and potentially eruptive) mass-loss during the final stages of stellar evolution is a key probe of poorly understood physics (e.g., Shiode & Quataert 2013; Smith & Arnett 2014) that sets the initial conditions to core-collapse.

Despite the steady increase in the number of events in the class of sub-luminous transients, the total number of well-studied events remain still small (≈ 10). An all-sky

two-day cadence survey with ZTF Phase II is ideally positioned to probe this rare population over a sufficiently large volume (given the deeper limiting magnitude of ZTF compared to other ongoing time domain surveys) to address questions regarding their intrinsic properties such as luminosity functions, spectroscopic diversity and ejecta mass distributions of the different sub-types and their volumetric rates. As likely tracers of the end points of white dwarfs and massive stars in extreme binary systems, their intrinsic rates are not only important from the point of view of understanding these rare transient phenomena but also have direct implications for current and future experiments in the field of gravitational wave astronomy. With a higher cadence than the nominal 3-day public survey in Phase I, the 2-day cadence in g and r bands will be particularly sensitive to the population of fastest transients in the local universe, of which only a handful are known, while the two-color coverage will also be a powerful diagnostic of the intrinsic color of these events.

wide-field optical surveys.

disminutive

see helium – less stripped compared with iPTF14gqr

Appendix A UV and Optical Photometry

A.1 Data

Table 3. Optical and UV photometry for AT2019dge.

Date (JD)	Instrument	Filter	m	σ_m
58582.1544	LT+IOO	g	18.59	0.01
58582.1552	LT+IOO	r	18.84	0.02
58582.1575	LT+IOO	i	19.11	0.02
58582.1583	LT+IOO	z	19.28	0.07
58583.1637	LT+IOO	g	18.48	0.02
58583.1645	LT+IOO	r	18.63	0.01
58584.2324	LT+IOO	g	18.58	0.01
58584.2332	LT+IOO	r	18.68	0.02
58584.2355	LT+IOO	i	18.85	0.02
58584.2363	LT+IOO	z	19.15	0.07
58590.0252	LT+IOO	g	19.47	0.14
58590.0260	LT+IOO	r	19.16	0.04
58590.0268	LT+IOO	i	19.24	0.07
58590.0277	LT+IOO	z	19.28	0.21
58591.0676	LT+IOO	g	19.44	0.07
58591.0685	LT+IOO	r	19.31	0.09
58591.0693	LT+IOO	i	19.22	0.06
58591.0701	LT+IOO	z	19.10	0.12
58592.0472	LT+IOO	g	19.40	0.13
58592.0472	LT+IOO	r	19.26	0.12
58592.0489	LT+IOO	i	19.27	0.10
58592.0497	LT+IOO	z	19.33	0.17
58593.1109	LT+IOO	r	19.41	0.06
58593.1117	LT+IOO	i	19.41	0.08
58593.1125	LT+IOO	z	19.46	0.12
58594.1142	LT+IOO	g	19.69	0.20
58594.1150	LT+IOO	r	19.50	0.08
58594.1158	LT+IOO	i	19.48	0.08
58594.1167	LT+IOO	z	19.52	0.16
58595.0926	LT+IOO	g	19.82	0.10
58595.0935	LT+IOO	r	19.60	0.07
58595.0943	LT+IOO	i	19.45	0.07
58595.0951	LT+IOO	z	19.55	0.11
58596.1380	LT+IOO	g	20.10	0.11
58596.1388	LT+IOO	r	19.75	0.06
58596.1396	LT+IOO	i	19.66	0.08
58596.1405	LT+IOO	z	19.71	0.16
58597.1508	LT+IOO	g	20.12	0.07
58597.1516	LT+IOO	r	19.77	0.05
58597.1539	LT+IOO	i	19.69	0.07
58597.1547	LT+IOO	z	19.95	0.15
58598.1207	LT+IOO	g	20.37	0.17
58598.1218	LT+IOO	r	19.89	0.06
58598.1247	LT+IOO	i	19.73	0.08
58598.1257	LT+IOO	z	20.13	0.30
58599.1894	LT+IOO	g	20.42	0.08

Table 3 *continued*

Table 3 *(continued)*

Date (JD)	Instrument	Filter	m	σ_m
58599.1918	LT+IOO	z	20.17	0.12
58601.1606	LT+IOO	i	20.38	0.10
58607.0861	LT+IOO	r	21.22	0.11
58607.0890	LT+IOO	i	20.88	0.10
58607.0900	LT+IOO	z	20.72	0.16
58610.1965	LT+IOO	g	21.86	0.19
58610.1974	LT+IOO	r	21.36	0.21
58610.1982	LT+IOO	i	21.28	0.19
58610.1990	LT+IOO	z	20.92	0.42
58611.1743	LT+IOO	g	21.77	0.23
58611.1751	LT+IOO	r	21.52	0.19
58611.1759	LT+IOO	i	21.10	0.12
58611.1767	LT+IOO	z	20.72	0.21
58580.4421	P48+ZTF	g	20.83	0.15
58581.4807	P48+ZTF	g	18.81	0.03
58582.4396	P48+ZTF	g	18.50	0.02
58583.4082	P48+ZTF	g	18.52	0.04
58584.4691	P48+ZTF	g	18.65	0.02
58586.4480	P48+ZTF	g	19.04	0.02
58587.4658	P48+ZTF	g	19.18	0.03
58588.4794	P48+ZTF	g	19.39	0.04
58591.3740	P48+ZTF	g	19.68	0.15
58592.4784	P48+ZTF	g	19.50	0.10
58593.4841	P48+ZTF	g	19.78	0.17
58596.4781	P48+ZTF	g	20.11	0.08
58597.4728	P48+ZTF	g	20.53	0.18
58599.2766	P48+ZTF	g	20.47	0.08
58612.4016	P48+ZTF	g	21.78	0.22
58616.4688	P48+ZTF	g	21.66	0.16
58580.4842	P48+ZTF	r	20.89	0.14
58581.4308	P48+ZTF	r	19.19	0.05
58582.4516	P48+ZTF	r	18.76	0.02
58584.4009	P48+ZTF	r	18.69	0.02
58585.4191	P48+ZTF	r	18.75	0.03
58586.4101	P48+ZTF	r	18.92	0.03
58587.4222	P48+ZTF	r	19.02	0.05
58588.4300	P48+ZTF	r	19.10	0.03
58589.3489	P48+ZTF	r	18.99	0.20
58591.4525	P48+ZTF	r	19.31	0.05
58592.3880	P48+ZTF	r	19.46	0.13
58593.4315	P48+ZTF	r	19.44	0.06
58596.3929	P48+ZTF	r	19.68	0.05
58597.4050	P48+ZTF	r	19.85	0.06
58598.3610	P48+ZTF	r	19.96	0.09
58599.4846	P48+ZTF	r	19.97	0.06
58600.4715	P48+ZTF	r	20.08	0.10
58605.4333	P48+ZTF	r	20.73	0.08
58607.3705	P48+ZTF	r	20.69	0.09
58608.4033	P48+ZTF	r	20.64	0.13
58612.4549	P48+ZTF	r	21.23	0.11
58616.4117	P48+ZTF	r	20.94	0.09
58617.3380	P48+ZTF	r	21.02	0.17
58627.3911	P48+ZTF	r	21.58	0.21
58635.3518	P48+ZTF	r	21.95	0.19

Table 3 *continued*

Table 3 *(continued)*

Date (JD)	Instrument	Filter	m	σ_m
58581.5163	P48+ZTF	i	19.44	0.17
58586.5159	P48+ZTF	i	18.98	0.08
58596.3822	P48+ZTF	i	19.66	0.16
58637.8263	P48+ZTF	r	22.27	0.16
58642.3119	P48+ZTF	r	22.40	0.17
58582.8289	*Swift*+UVOT	B	18.68	0.40
58582.8280	*Swift*+UVOT	U	18.80	0.10
58582.8346	*Swift*+UVOT	$UVM2$	18.55	0.07
58582.8261	*Swift*+UVOT	$UVW1$	18.61	0.19
58582.8299	*Swift*+UVOT	$UVW2$	18.68	0.11
58582.8337	*Swift*+UVOT	V	18.29	0.11
58583.5775	*Swift*+UVOT	B	18.46	0.29
58583.5766	*Swift*+UVOT	U	19.22	0.10
58583.5833	*Swift*+UVOT	$UVM2$	18.85	0.09
58583.5747	*Swift*+UVOT	$UVW1$	18.49	0.14
58583.5785	*Swift*+UVOT	$UVW2$	18.87	0.10
58583.5823	*Swift*+UVOT	V	18.51	0.11

NOTE—m and σ_m are observed magnitude (without extinction correction) in AB system.

Table 4. Photometry of the host galaxy

Instrument/Filter	$\lambda_{\rm eff}$ (Å)	m	σ_m
UVOT/$UVW2$	2079.0	20.492	0.124
UVOT/$UVM2$	2255.1	20.471	0.172
UVOT/$UVW1$	2614.2	20.081	0.155
UVOT/U	3475.5	19.631	0.145
UVOT/B	4359.1	18.812	0.139
UVOT/V	5430.1	18.194	0.171
SDSS/u'	3561.8	19.636	0.082
SDSS/g'	4718.9	18.540	0.015
SDSS/r'	6185.2	18.056	0.026
SDSS/i'	7499.7	17.885	0.028
SDSS/z'	8961.5	17.697	0.089
PS1/$g_{\rm PS1}$	4866.5	18.538	0.042
PS1/$r_{\rm PS1}$	6214.6	18.029	0.030
PS1/$i_{\rm PS1}$	7544.6	17.845	0.033
PS1/$z_{\rm PS1}$	8679.5	17.755	0.050
PS1/$y_{\rm PS1}$	9633.3	17.710	0.063
2MASS/J	12410.5	17.653	0.215
2MASS/H	16513.7	17.690	0.420
WISE/$W1$	34002.6	18.460	0.069
WISE/$W2$	46520.1	18.953	0.136

NOTE—m and σ_m are observed magnitude (without extinction correction) in AB system.

The full set of photometry of AT2019dge is listed in Table 3. Photometry of the host galaxy SDSS J173646.73+503252.3 is listed in Table 4.

In Figure A1 we show the photometry interpolated onto common epochs, and fit to a blackbody function to derive the photospheric evolution (see Section 3.1). The resulting evolution in bolometric lumonosity, pho-

tospheric radius, and effective temperatures is listed in Table 5

Table 5. Physical evolution of AT2019dge from blackbody fits.

Δt	$L(10^{41}\,{\rm erg\,s^{-1}})$	$R\ (10^3\,R_\odot)$	$T\ (10^3\,{\rm K})$
-2.74	1.78	2.23	10.08
-1.72	$45.83^{+49.11}_{-16.74}$	$2.18^{+0.45}_{-0.48}$	$23.01^{+8.21}_{-4.31}$
-0.66	$27.17^{+1.13}_{-1.08}$	$3.48^{+0.08}_{-0.08}$	$15.97^{+0.34}_{-0.33}$
0.27	$19.26^{+0.76}_{-0.73}$	$4.92^{+0.14}_{-0.14}$	$12.32^{+0.29}_{-0.29}$
1.10	$15.72^{+0.46}_{-0.42}$	$5.39^{+0.14}_{-0.14}$	$11.20^{+0.23}_{-0.22}$
3.26	$8.34^{+0.22}_{-0.20}$	$7.27^{+0.46}_{-0.44}$	$8.22^{+0.31}_{-0.28}$
4.24	7.25	7.37	7.89
5.25	6.09	8.81	6.90
6.83	$6.16^{+0.63}_{-0.45}$	$7.12^{+1.02}_{-0.92}$	$7.70^{+0.74}_{-0.62}$
7.98	$5.28^{+0.23}_{-0.21}$	$8.02^{+0.76}_{-0.70}$	$6.98^{+0.39}_{-0.35}$
8.98	$5.48^{+0.43}_{-0.35}$	$6.86^{+0.95}_{-0.87}$	$7.61^{+0.65}_{-0.55}$
10.05	$4.53^{+0.35}_{-0.26}$	$7.49^{+1.04}_{-0.95}$	$6.95^{+0.61}_{-0.51}$
10.92	$4.47^{+0.64}_{-0.44}$	$6.70^{+1.24}_{-1.09}$	$7.32^{+0.93}_{-0.74}$
11.89	$4.03^{+0.24}_{-0.21}$	$7.49^{+0.83}_{-0.76}$	$6.75^{+0.45}_{-0.40}$
13.06	$3.34^{+0.10}_{-0.10}$	$7.55^{+0.69}_{-0.64}$	$6.42^{+0.31}_{-0.29}$
14.05	$3.08^{+0.10}_{-0.09}$	$7.09^{+0.63}_{-0.58}$	$6.49^{+0.31}_{-0.28}$
14.97	$2.82^{+0.14}_{-0.12}$	$7.38^{+1.23}_{-1.07}$	$6.21^{+0.57}_{-0.48}$
16.09	$2.45^{+0.09}_{-0.09}$	$6.19^{+0.59}_{-0.57}$	$6.56^{+0.33}_{-0.29}$
23.96	$1.02^{+0.06}_{-0.06}$	$5.59^{+1.27}_{-1.11}$	$5.53^{+0.70}_{-0.53}$
27.00	$0.73^{+0.08}_{-0.08}$	$4.25^{+1.30}_{-1.06}$	$5.81^{+0.88}_{-0.68}$
27.98	$0.79^{+0.07}_{-0.06}$	$5.95^{+1.79}_{-1.34}$	$5.01^{+0.66}_{-0.57}$
29.23	0.84	5.94	5.13
33.24	1.03	6.03	5.35

A.2 Modelling Early Light Curve

Table 6. Shock cooling model parameters θ and their priors

θ	Description	Prior
$\lg R_{\rm ext}$	$\log_{10}$ of extented material radius in cm	$\mathcal{U}(-5, 25)$
$\lg M_{\rm ext}$	$\log_{10}$ of extented material mass in $M_\odot$	$\mathcal{U}(-4, 0)$
$t_{\rm fl}$	first light epoch in MJD relative to 58583.2	$\mathcal{U}(-8, -2.76)$
E_{51}	SN energy divided by $10^{51}\,{\rm erg\,s^{-1}}$	$\mathcal{U}(0.01, 10)$
$E_{\rm ext,49}$	$E_{\rm ext}$ divided by $10^{49}\,{\rm erg\,s^{-1}}$	$\mathcal{U}(0.1, 100)$

We cast the P15 analytical expression for the shape of the early-time light curve in terms of $M_{\rm ext}$, $R_{\rm ext}$, $E_{\rm ext}$,
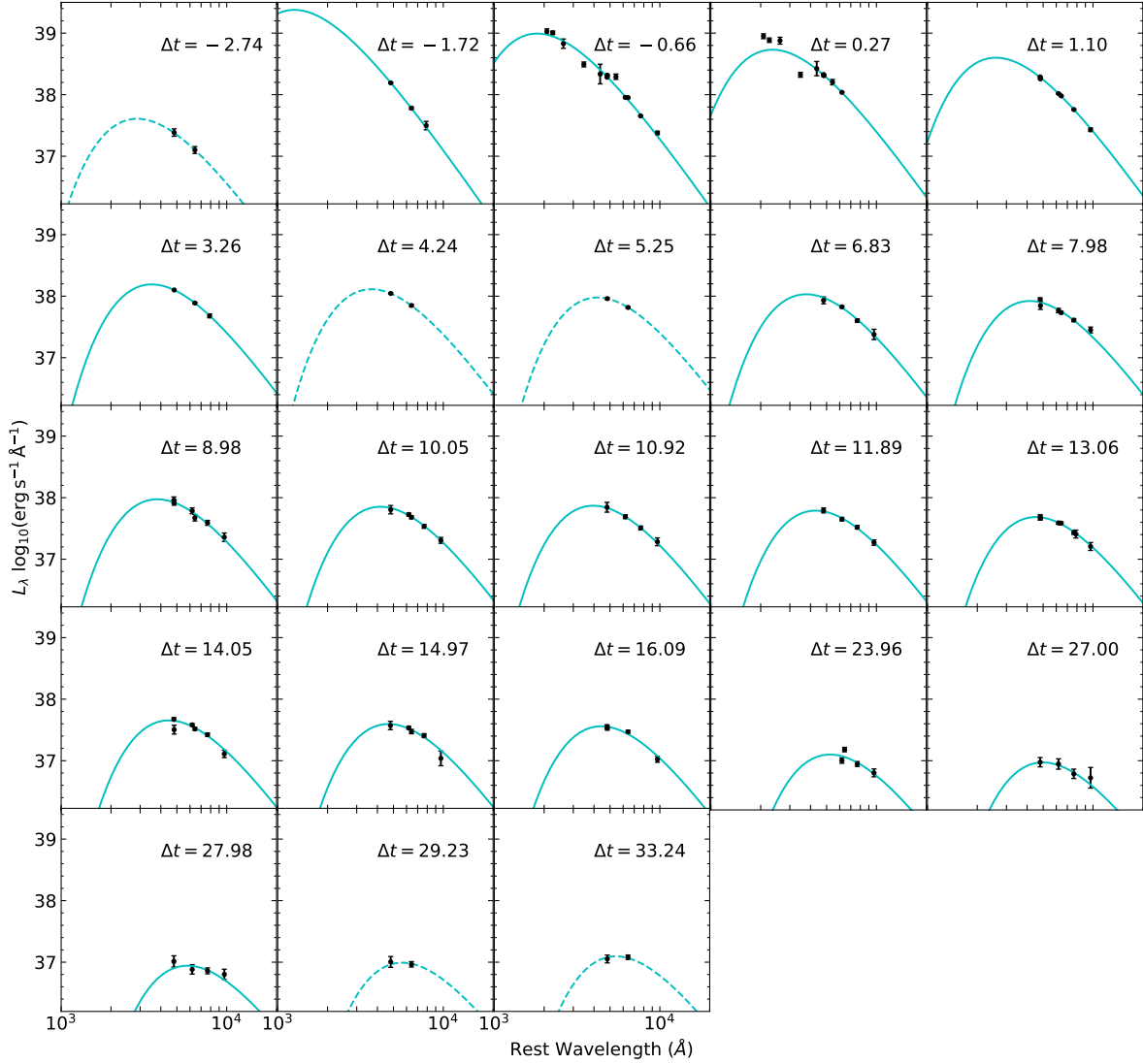
Figure A1. Black data points are $Swift$/UVOT and optical photometry of AT2019dge. Solid lines show the maximum MCMC a posteriori model fits. Dashed lines are simple χ^2 fits.

and E_{51}:

$$L(t) = \frac{t_e E_{\rm ext}}{t_p^2}\exp\left[-\frac{t(t+2t_e)}{2t_p^2}\right]\,{\rm erg\,s}^{-1} \qquad {\rm (A1a)}$$

$$t_e = 10^{-9}R_{\rm ext}E_{{\rm ext},49}^{-1/2}\left(\frac{M_{\rm ext}}{0.01M_\odot}\right)^{1/2}\,{\rm s} \qquad {\rm (A1b)}$$

$$t_p = 1.1\times10^5\kappa_{34}^{1/2}E_{51}^{-0.01/1.4}$$
$$\times E_{{\rm ext},49}^{-0.17/0.7}\left(\frac{M_{\rm ext}}{0.01M_\odot}\right)^{0.74}\,{\rm s} \qquad {\rm (A1c)}$$

where t is time since explosion in seconds, $\kappa_{34} = \kappa/(0.34\,{\rm cm^2\,g^{-1}})$, $E_{{\rm ext},49} = E_{\rm ext}/(10^{49}\,{\rm erg\,s^{-1}})$, $E_{51} = E/(10^{51}\,{\rm erg\,s^{-1}})$, and E is energy of the explosion. Following P15 we assume the emission is a blackbody at

radius

$$R(t) = R_{\rm ext} + 10^9\left(\frac{E_{\rm ext}}{10^{49}\,{\rm erg\,s^{-1}}}\right)^{1/2}\left(\frac{M_{\rm ext}}{0.01M_\odot}\right)^{-0.5}t$$

and temperature

$$T(t) = \left(\frac{L(t)}{4\pi R(t)^2\sigma_{\rm SB}}\right)^{1/4}$$

We fix $\kappa \approx 0.2\,{\rm cm^2\,g^{-1}}$ as appropriate for a hydrogen-deficient ionized gas, and assign wide flat priors for all model parameters, as summarized in Table 6. We only include observations up to $\Delta t = 2\,{\rm d}$ in the fitting. We found that this particular choice of Δt — 2 d instead of 1 d or 3 d — in general does not affect the final inference for the model parameters. Figure A2 shows the corner
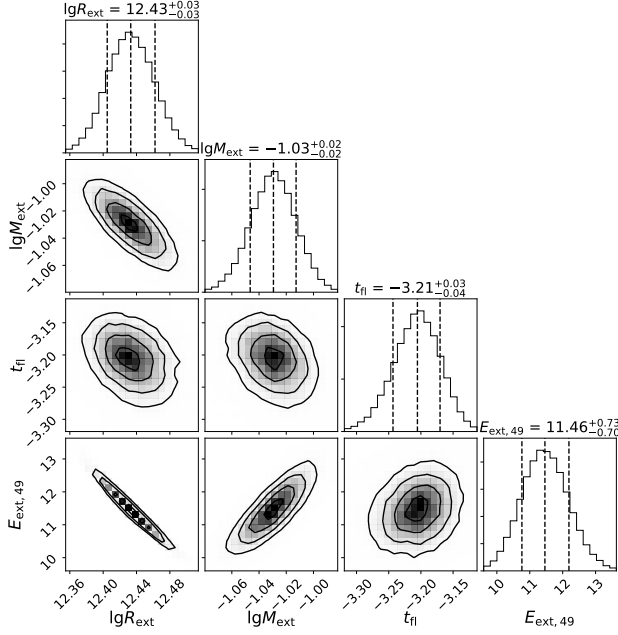
Figure A2. Corner plot showing the posterior constraints on $\lg R_{\rm ext}$, $\lg M_{\rm ext}$, $t_{\rm fl}$, and $E_{\rm ext,49}$. Marginalized one-dimensional distributions are shown along the diagonal, along with the median estimate and the 68% credible region (shown with vertical dashed lines).

plot of $\lg R_{\rm ext}$, $\lg M_{\rm ext}$, $t_{\rm fl}$, and $E_{\rm ext,49}$. For clarity, E_{51} is excluded as it does not exhibit strong covariance with the parameters shown here. This can be understood by Eq. A1c, which gives $t_p \propto E_{51}^{-0.01/1.4}$, suggesting that the shock cooling luminosity only weakly depends on E_{51}.

The maximum a posteriori model is visualized by solid lines in Figure A3 color-coded in different filters. Note that the fitting is not perfect at the UV bands since the SED is not exactly a blackbody at peak (see Figure A1). The rising part of the model does not closely match to data due to the ignorance of the density structure of the stellar profile. Nevertheless, the peak of the light curve is well captured by this model.

A.3 Modelling the Main Peak

For $^{56}{\rm Ni} \rightarrow^{56} {\rm Co} \rightarrow^{56} {\rm Fe}$ decay powered explosions, the energy deposition rate is

$$\varepsilon_{\rm rad} = \varepsilon_{\rm Ni,\gamma}(t) + \varepsilon_{\rm Co,\gamma}(t) \tag{A2}$$

$$\varepsilon_{\rm Ni,\gamma}(t) = \epsilon_{\rm Ni} e^{-t/\tau_{\rm Ni}} \tag{A3}$$

$$\varepsilon_{\rm Co,\gamma}(t) = \epsilon_{\rm Co} \left(e^{-t/\tau_{\rm Co}} - e^{-t/\tau_{\rm Ni}} \right) \tag{A4}$$

where $\epsilon_{\rm Ni} = 3.90 \times 10^{10}\,{\rm erg\,g^{-1}\,s^{-1}}$, $\epsilon_{\rm Co} = 6.78 \times 10^{9}\,{\rm erg\,g^{-1}\,s^{-1}}$, $\tau_{\rm Ni} = 8.8\,{\rm d}$ and $\tau_{\rm Co} = 111.3\,{\rm d}$ are the decay lifetimes of ^{56}Ni and ^{56}Co (Nadyozhin 1994). The
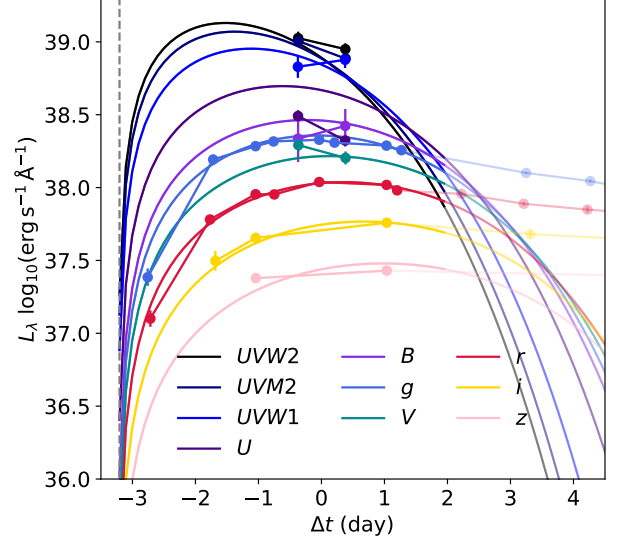

Figure A3. Cooling emission model fit to the early light curve of AT2019dge. Data excluded from the fitting are shown as transparent circles. The maximum a posteriori model is shown via solid lines. The vertical dashed line shows the median 1-D marginalized posterior value of $t_{\rm fl}$.

effective heating rate is modified by the probability of thermalization, and thus $\varepsilon_{\rm heat} \leq \varepsilon_{\rm rad}$.

The bolometric light curve can be generally divided into the photospheric phase and the nebula phase. The photospheric phase can be modelled using Equations given in Valenti et al. (2008, Appendix A), with modifications given by Lyman et al. (2016, Eq. 3),

$$L_{\rm phot}(t) = M_{\rm Ni} e^{-x^2} \times$$
$$\left[(\epsilon_{\rm Ni} - \epsilon_{\rm Co}) \int_0^x (2ze^{-2zy+z^2}){\rm d}z \right.$$
$$\left. + \epsilon_{\rm Co} \int_0^x (2ze^{-2zy+2zs+z^2}){\rm d}z \right] \tag{A5}$$

where $x = t/\tau_{\rm m}$, $y = \tau_{\rm m}/(2\tau_{\rm Ni})$,

$$s = \frac{\tau_{\rm m}(\tau_{\rm Co} - \tau_{\rm Ni})}{2\tau_{\rm Co}\tau_{\rm Ni}},$$

$$\tau_{\rm m} = \left(\frac{2\kappa_{\rm opt}M_{\rm ej}}{13.8cv_{\rm phot}} \right)^{1/2} \tag{A6}$$

At the nebula phase the SN ejecta becomes optically thin, such that the delay between the energy deposition from radioactivity and the optical radiation becomes shorter. The bolometric luminosity is then equal to the rate of energy deposition: $L_{\rm neb}(t) = Q(t)$. At any given time, the energy deposition rate $Q(t)$ is (Wheeler et al. 2015; Wygoda et al. 2019):

$$Q(t) \approx Q_\gamma(t) \left(1 - e^{-(t_0/t)^2} \right) \tag{A7}$$

where $Q_\gamma(t) = M_{\mathrm{Ni}}\varepsilon_{\mathrm{rad}}$ is the energy release rate of gamma-rays, t_0 is the time at which the ejecta becomes optically thin to gamma rays. Here the difference between energy deposition rate of gamma-rays and positrons is neglected.
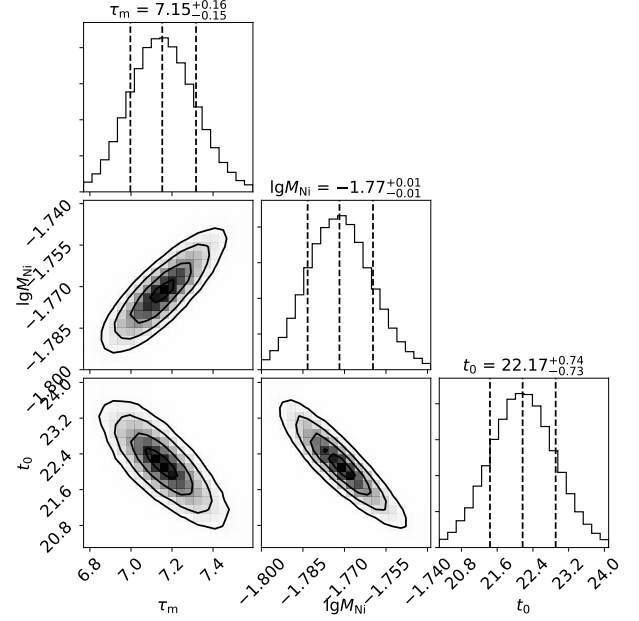

Figure A4. Corner plot showing the posterior constraints on τ_{m}, $\lg M_{\mathrm{Ni}}$, and t_0. Marginalized one-dimensional distributions are shown along the diagonal, along with the median estimate and the 68% credible region (shown with vertical dashed lines).

Table 7. ^{56}Ni decay model parameters θ and their priors

θ	Description	Prior
τ_{m}	characteristic photon diffusion time in day	$\mathcal{U}(1, 20)$
$\lg M_{\mathrm{Ni}}$	$\log_{10}$ of nickel mass in $M_\odot$	$\mathcal{U}(-4, 0)$
t_0	characteristic γ-ray escape time in day	$\mathcal{U}(1, 100)$

To fit the shock cooling subtracted bolometric light curve with a simple radioactive decay model, we do not divide the data into photosperic phase and nebula phase, but instead adopt the following formula for the whole light curve:

$$L(t) = L_{\mathrm{phot}}(t) \left(1 - e^{-(t_0/t)^2}\right) \qquad \text{(A8)}$$

Priors or the model parameters are summarized in Table 7, and Figure A4 shows the coner plot of τ_{m}, $\lg M_{\mathrm{Ni}}$, and t_0.

Appendix B UV and Optical Spectroscopy

B.1 Data

The log of UV and optical spectroscopy is presented in Table 8.

We use line centers of nebular lines to derive the spectroscopic redshift of the host (Table 9). The mean of all centroids gives $z = 0.0213 \pm 0.0001$.

References

Abbott, B. P., Abbott, R., Abbott, T. D., et al. 2018, Living Reviews in Relativity, 21, 3

Alam, S., Albareti, F. D., Allende Prieto, C., et al. 2015, ApJS, 219, 12

Arcavi, I., Hosseinzadeh, G., Brown, P. J., et al. 2017, ApJL, 837, L2

Arnett, W. D. 1982, ApJ, 253, 785

Astropy Collaboration, Robitaille, T. P., Tollerud, E. J., et al. 2013, A&A, 558, A33

Table 8. Log of AT2019dge spectroscopy.

Start Time	Instrument	Δt	Exposure Time	Airmass	Resolution
(UTC)		(day)	(s)		(FWHM $\mathring{A}$)
2019 Apr 09 03:30:28	LT+SPART	-1.1	500	1.800	18
2019 Apr 10 03:06:10	LT+SPART	-0.1	500	1.800	18
2019 Apr 10 14:21:44	Keck1+LRIS	$+0.4$	300	1.169	6
2019 Apr 22 05:08:00	HST+WFC3+UVIS	$+12.0$	2×250	—	43
2019 Apr 24 11:06:43	P200+DBSP	$+14.3$	1200	1.047	3–5
2019 Jul 04 11:49:18	Keck1+LRIS	$+85.3$	1740	1.421	6
2019 Aug 31 08:04:58	Keck1+LRIS	$+143.1$	1150	1.409	6
2019 Sep 28 08:14:27	Keck1+LRIS	$+171.1$	600	2.165	6
2020 Feb 18 15:23:40	Keck1+LRIS	$+314.4$	1450	1.384	6

Table 9. Line fluxes from the host galaxy of AT2019dge extracted from the Keck/LRIS spectrum obtained on Aug xx 2019.

Transition	λ_{obs}	F
	(Å)	(10^{-16} erg cm^{-2} s^{-1})
Hβ	4862.35 ± 0.21	32.45 ± 2.08
[O III]$\lambda5007$	5007.06 ± 0.55	67.56 ± 13.52
Hα	6562.07 ± 0.03	115.79 ± 1.16
[N II]$\lambda6583$	6582.62 ± 0.08	8.89 ± 0.37

Note—All measurements are corrected for Galactic reddening.

Barnsley, R. M., Smith, R. J., & Steele, I. A. 2012, AN, 333, 101

Bellm, E. C., & Sesar, B. 2016, pyraf-dbsp: Reduction pipeline for the Palomar Double Beam Spectrograph

Bellm, E. C., Kulkarni, S. R., Graham, M. J., et al. 2019a, PASP, 131, 018002

Bellm, E. C., Kulkarni, S. R., Barlow, T., et al. 2019b, PASP, 131, 068003

Boquien, M., Burgarella, D., Roehlly, Y., et al. 2019, A&A, 622, A103

Bruzual, G., & Charlot, S. 2003, MNRAS, 344, 1000

Bufano, F., Immler, S., Turatto, M., et al. 2009, ApJ, 700, 1456

Calzetti, D., Armus, L., Bohlin, R. C., et al. 2000, ApJ, 533, 682

Cardelli, J. A., Clayton, G. C., & Mathis, J. S. 1989, ApJ, 345, 245

Chabrier, G. 2003, PASP, 115, 763

Chen, P., Dong, S., Stritzinger, M. D., et al. 2020, ApJL, 889, L6

Chevalier, R. A. 1982, ApJ, 259, 302

—. 1998, ApJ, 499, 810

Chugai, N. N., & Danziger, I. J. 1994, MNRAS, 268, 173

De, K., Kasliwal, M. M., Cantwell, T., et al. 2018a, ApJ, 866, 72

De, K., Kasliwal, M. M., Ofek, E. O., et al. 2018b, Science, 362, 201

Dessart, L., Hillier, D. J., Li, C., & Woosley, S. 2012, MNRAS, 424, 2139

Draine, B. T., & Li, A. 2007, ApJ, 657, 810

Drout, M. R., Soderberg, A. M., Gal-Yam, A., et al. 2011, ApJ, 741, 97

Drout, M. R., Soderberg, A. M., Mazzali, P. A., et al. 2013, ApJ, 774, 58

Filippenko, A. V., & Sargent, W. L. W. 1989, ApJL, 345, L43

Foreman-Mackey, D. 2016, JOSS, 24

Foreman-Mackey, D., Hogg, D. W., Lang, D., & Goodman, J. 2013, Publications of the Astronomical Society of the Pacific, 125, 306

Fremling, C., Sollerman, J., Taddia, F., et al. 2016, A&A, 593, A68

Fremling, C., Ko, H., Dugas, A., et al. 2019, ApJL, 878, L5

Fruchter, A. S. 2018, A New Approach to Following Transients with HST: Rolling Snapshots, HST Proposal, HST Proposal

Gal-Yam, A., Bufano, F., Barlow, T. A., et al. 2008, ApJL, 685, L117

Gal-Yam, A., Arcavi, I., Ofek, E. O., et al. 2014, Nature, 509, 471

Gehrels, N., Chincarini, G., Giommi, P., et al. 2004, ApJ, 611, 1005

Graham, M. J., Kulkarni, S. R., Bellm, E. C., et al. 2019, arXiv

Guillochon, J., Parrent, J., Kelley, L. Z., & Margutti, R. 2017, ApJ, 835, 64

Hamuy, M., Maza, J., Pinto, P. A., et al. 2002, AJ, 124, 417

Ho, A. Y. Q., Phinney, E. S., Ravi, V., et al. 2019a, ApJ, 871, 73

Ho, A. Y. Q., Goldstein, D. A., Schulze, S., et al. 2019b, ApJ, 887, 169

Ho, P. T. P., Moran, J. M., & Lo, K. Y. 2004, ApJL, 616, L1

Horesh, A., Stockdale, C., Fox, D. B., et al. 2013, MNRAS, 436, 1258

Hosseinzadeh, G., Arcavi, I., Valenti, S., et al. 2017, ApJ, 836, 158

Hunter, J. D. 2007, Computing In Science & Engineering, 9, 90

Jeffery, D. J., Kirshner, R. P., Challis, P. M., et al. 1994, ApJL, 421, L27

Jones, E., Oliphant, T., Peterson, P., et al. 2001–, SciPy: Open source scientific tools for Python

Kasen, D. 2017, Unusual Supernovae and Alternative Power Sources, ed. A. W. Alsabti & P. Murdin, 939

Kasliwal, M. M., Kulkarni, S. R., Gal-Yam, A., et al. 2010, ApJL, 723, L98

—. 2012, ApJ, 755, 161

Kasliwal, M. M., Cannella, C., Bagdasaryan, A., et al. 2019, PASP, 131, 038003

Kennicutt, Robert C., J. 1998, ApJ, 498, 541

Khatami, D. K., & Kasen, D. N. 2019, ApJ, 878, 56

Khazov, D., Yaron, O., Gal-Yam, A., et al. 2016, ApJ, 818, 3

Kleiser, I., Fuller, J., & Kasen, D. 2018a, MNRAS, 481, L141

Kleiser, I. K. W., & Kasen, D. 2014, MNRAS, 438, 318

Kleiser, I. K. W., Kasen, D., & Duffell, P. C. 2018b, MNRAS, 475, 3152

Komatsu, E., Smith, K. M., Dunkley, J., et al. 2011, ApJS, 192, 18

Leibundgut, B., Kirshner, R. P., Pinto, P. A., et al. 1991, ApJ, 372, 531

Liu, Y.-Q., Modjaz, M., Bianco, F. B., & Graur, O. 2016, ApJ, 827, 90

Luridiana, V., Morisset, C., & Shaw, R. A. 2013, PyNeb: Analysis of emission lines

Lyman, J. D., Bersier, D., James, P. A., et al. 2016, MNRAS, 457, 328

Madau, P., & Dickinson, M. 2014, ARA&A, 52, 415

Margalit, B., & Metzger, B. D. 2016, MNRAS, 461, 1154

Marino, R. A., Rosales-Ortega, F. F., Sánchez, S. F., et al. 2013, A&A, 559, A114

Masci, F. J., Laher, R. R., Rusholme, B., et al. 2019, PASP, 131, 018003

Matheson, T., Filippenko, A. V., Ho, L. C., et al. 2000, AJ, 120, 1499

Matheson, T., Filippenko, A. V., Li, W., et al. 2001, AJ, 121, 1648

Mazzali, P. A., Sullivan, M., Hachinger, S., et al. 2014, MNRAS, 439, 1959

McBrien, O. R., Smartt, S. J., Chen, T.-W., et al. 2019, ApJL, 885, L23

McKinney, W. 2010, 51

Metzger, B. D., Piro, A. L., & Quataert, E. 2009, MNRAS, 396, 1659

Modjaz, M., Gutiérrez, C. P., & Arcavi, I. 2019, NatAs, 3, 717

Moriya, T. J., Mazzali, P. A., Tominaga, N., et al. 2017, MNRAS, 466, 2085

Nadyozhin, D. K. 1994, ApJS, 92, 527

Nakar, E., & Piro, A. L. 2014, ApJ, 788, 193

Nomoto, K., Yamaoka, H., Pols, O. R., et al. 1994, Nature, 371, 227

Ofek, E. O., Lin, L., Kouveliotou, C., et al. 2013, ApJ, 768, 47

Oke, J. B., & Gunn, J. E. 1982, PASP, 94, 586

Oke, J. B., Cohen, J. G., Carr, M., et al. 1995, PASP, 107, 375

Pastorello, A., Mattila, S., Zampieri, L., et al. 2008, MNRAS, 389, 113

Pastorello, A., Benetti, S., Brown, P. J., et al. 2015, MNRAS, 449, 1921

Patterson, M. T., Bellm, E. C., Rusholme, B., et al. 2019, PASP, 131, 018001

Perley, D. A. 2019, PASP, 131, 084503

Pettini, M., & Pagel, B. E. J. 2004, MNRAS, 348, L59

Piascik, A. S., Steele, I. A., Bates, S. D., et al. 2014, Society of Photo-Optical Instrumentation Engineers (SPIE) Conference Series, Vol. 9147, SPRAT: Spectrograph for the Rapid Acquisition of Transients, 91478H

Piro, A. L. 2015, ApJL, 808, L51

Poznanski, D., Chornock, R., Nugent, P. E., et al. 2010, Science, 327, 58

Prentice, S. J., Ashall, C., James, P. A., et al. 2019, MNRAS, 485, 1559

Rest, A., Garnavich, P. M., Khatami, D., et al. 2018, NatAs, 2, 307

Roming, P. W. A., Kennedy, T. E., Mason, K. O., et al. 2005, SSRv, 120, 95

Schlafly, E. F., & Finkbeiner, D. P. 2011, ApJ, 737, 103

Schlegel, D. J., Finkbeiner, D. P., & Davis, M. 1998, ApJ, 500, 525

Shen, K. J., Kasen, D., Weinberg, N. N., et al. 2010, ApJ, 715, 767

Shiode, J. H., & Quataert, E. 2014, ApJ, 780, 96

Shivvers, I., Zheng, W., Van Dyk, S. D., et al. 2017, MNRAS, 471, 4381

Shivvers, I., Filippenko, A. V., Silverman, J. M., et al. 2019, MNRAS, 482, 1545

Sim, S. A., Fink, M., Kromer, M., et al. 2012, MNRAS, 420, 3003

Smith, N. 2017, Interacting Supernovae: Types IIn and Ibn, ed. A. W. Alsabti & P. Murdin, 403

Smith, N., Li, W., Filippenko, A. V., & Chornock, R. 2011, MNRAS, 412, 1522

Smith, N., Mauerhan, J. C., Cenko, S. B., et al. 2015, MNRAS, 449, 1876

Steele, I. A., Smith, R. J., Rees, P. C., et al. 2004, Proc. SPIE, 5489, 679

Storey, P. J., & Hummer, D. G. 1995, MNRAS, 272, 41

Sullivan, M., Kasliwal, M. M., Nugent, P. E., et al. 2011, ApJ, 732, 118

Suwa, Y., Yoshida, T., Shibata, M., et al. 2015, MNRAS, 454, 3073

Taddia, F., Stritzinger, M. D., Bersten, M., et al. 2018, A&A, 609, A136

Tauris, T. M., Langer, N., Moriya, T. J., et al. 2013, ApJL, 778, L23

Tauris, T. M., Langer, N., & Podsiadlowski, P. 2015, MNRAS, 451, 2123

Tauris, T. M., Kramer, M., Freire, P. C. C., et al. 2017, ApJ, 846, 170

Valenti, S., Benetti, S., Cappellaro, E., et al. 2008, MNRAS, 383, 1485

Weiler, K. W., Williams, C. L., Panagia, N., et al. 2007, ApJ, 671, 1959

Wellons, S., Soderberg, A. M., & Chevalier, R. A. 2012, ApJ, 752, 17

Wheeler, J. C., Johnson, V., & Clocchiatti, A. 2015, MNRAS, 450, 1295

Whitesides, L., Lunnan, R., Kasliwal, M. M., et al. 2017, ApJ, 851, 107

Woosley, S. E. 2019, ApJ, 878, 49

Wygoda, N., Elbaz, Y., & Katz, B. 2019, MNRAS, 484, 3951

Yan, L., Quimby, R., Gal-Yam, A., et al. 2017, ApJ, 840, 57

Yao, Y., Miller, A. A., Kulkarni, S. R., et al. 2019, ApJ, 886, 152

Yaron, O., & Gal-Yam, A. 2012, PASP, 124, 668

Yaron, O., Perley, D. A., Gal-Yam, A., et al. 2017, Nature Physics, 13, 510

Yoon, S. C., Woosley, S. E., & Langer, N. 2010, ApJ, 725, 940